Implementation of a nonlinear controller in Phase-Locked Loop experiments for nonlinear structure identification

Augustus Chukwu, Cyrille Stephan, Cyril Touzé, Olivier Doaré

Implementation of a nonlinear controller in Phase-Locked Loop experiments for nonlinear structure identification

Augustus Chukwu[1,2], Cyrille Stephan[1], Cyril Touzé[2], and Olivier Doaré[2]

[1] DAAA, ONERA, Institut Polytechnique de Paris, 92320 Châtillon France
[2] ENSTA, Institut Polytechnique de Paris, 91120 Palaiseau France augustus.chukwu@onera.fr, cyrille.stephan@onera.fr, cyril.touze@ensta-paris.fr, olivier.doare@ensta-paris.fr

Abstract. Experimental continuation methods are used to retrieve and identify nonlinear characteristics of vibrating structures. Among the available methods, Phase-Locked Loop (PLL) allows for an easy-to-implement yet efficient method to continue nonlinear solutions such as backbone curves or frequency response functions. The PLL automatically locks onto the prescribed phase and thanks to a linear (proportional-integral) controller, can stabilize unstable periodic orbits. However, the tuning of the different parameters to be used in such a loop are seldomly documented in the literature, which in turn might lead to long duration tests. To ease the tuning effort and reduce the experimenting time, a nonlinear controller is here proposed as a way to improve the efficacy of Phase-Locked Loop testing. Thanks to the proposed design, named NCPLL (Nonlinear Controller PLL), most of the parameters are tuned easily, while a rapid locking to the prescribed state is at hand. The nonlinear gain can be easily adapted to reach a locked state rapidly. The efficacy of the NCPLL is first demonstrated on simple numerical examples including nonlinear oscillators with smooth restoring forces and Coulomb friction, and a finite element beam model with localized nonlinearities. Then the method is deployed on two different experimental test rigs. First, the case of smooth nonlinearity is tackled thanks to a cantilever beam vibrating in the magnetic field created by two magnets. Finally, the case of friction is addressed by considering an assembled beam with friction joints. In all the tested cases, the NCPLL shows excellent performance, requiring minimal tuning efforts whilst leading to fast measurements.

Keywords: Phase-Locked Loop · Experimental Continuation · Nonlinear Normal Modes · System Identification · Force Appropriation.

1 Introduction

In the field of vibration, identification has always been an important topic, making the link between numerical models and experiments. For linear vibrations, the methods are nowadays considered as mature and used routinely in engineering applications [10,44,4]. Considering nonlinear vibrations make the picture more complex because of the number of possible solutions, including not only periodic solutions but also quasi-periodic and chaotic oscillations, and the appearance of unstable solutions through bifurcations [31,14]. This variety of solutions gave rise in turn to a diversity of methods for nonlinear structural identification [20,32].

In recent years, a decisive progress in experimental testing of nonlinear structures have been made with the advent of experimental continuation methods. By drawing a parallel with numerical continuation techniques that have shown remarkable results for the analysis of nonlinear systems, experimental continuation relies on feedback stabilization in order to continue both stable and unstable states of a given system [42], hence giving access to a full picture of the possible dynamical solutions. Two main control-based techniques are today available for experimental continuation: control-based continuation (CBC) [43,36], and Phase-Locked Loop (PLL) [27,33]. They have already been used in a variety of different contexts, *e.g.* for the identification of structures with well-separated modes and the measurement of the primary resonance [28,8,2,34,7], with modal interactions [13,37,12,8], to detect secondary resonances [51] or for application to friction nonlinearity [39], and also to unfold isolated branches of solutions [50]. Interestingly, the two methods are compared on the case of a structure featuring frictional nonlinearity [1]. A recent review paper offers a comprehensive overview of the achievements made to date [35].

Applications of continuation methods to engineering structures, however, still remain rarely documented in archival literature [40]. Indeed, most of the papers up to now focused on developing the methods and highlighting their ability in dealing with different nonlinear phenomena, such that most of the applications consider simple structures such as beams and plates, or lumped structures with localized nonlinearity [48,30,7]. The next step of the development is thus to target applications to large-scale engineering structures. In aeronautics, Ground Vibration Test (GVT) for aircraft structure identification could gain in incorporating experimental continuation techniques in their usual development to provide a deeper insight to the nonlinear behaviour of aircrafts. Furthermore, current GVT tools rely on manual operation and top expertise which pose a challenge in terms of testing time and available know-how. Note that a first application of experimental continuation to a full aircraft has been recently reported in [52].

Now focusing more specifically on the case of PLL, the method gained popularity for tracking the resonant and anti-resonant responses of nonlinear systems to a harmonic excitation since the pioneering works [46,28,33]. Stability analysis of a PLL controlled experiment reveals that the performance of the controller is influenced by structural damping [11,8]. A full stability analysis of the auto-resonant system (composed of the PLL and the structure) requires the knowledge of the nonlinearity in the structure. For engineering applications, the nonlinearity is generally unknown and part of the identification procedure, such that tuning methods based on a priori knowledge of the nonlinearity are difficult to apply in practice. The tuning of the parameters of the PLL is thus, following the published literature, mostly heuristic, which is an obstacle to its fast use and mastering in a variety of engineering contexts. First proposals for the tuning can be found for example in [8,49,17]. In [8], the dynamics of the system is modeled as a Duffing oscillator and provided to be the best model in the case of geometrical nonlinearities. Criteria for the tuning of the gains of the Proportional-Integral (PI) controller are derived to stabilize the unstable part of the Frequency- response Curve (FRC), while the measurement is realized with a continuous sweep (either of the force or the phase). Linear vibration and the interaction with the shaker are considered in [17]. Heuristic tuning can thus contribute to the duration of the testing, while suboptimal tuning also leads to longer experimental tests, which might in turn lead to structural fatigue [24], a feature that one would like to avoid in general. Therefore, optimizing the duration test is an important pre-requisite for wider application of PLL to engineering problems.

Motivated by recent developments and challenges, this work tackles some limitations of PLL design related to the parameters tuning and the duration of the experiment. More specifically, a nonlinear controller is implemented in the PLL in replacement of the usual linear proportional controller, Section 2. It is shown that, though the addition of the nonlinear controller leads to more number of parameters to be tuned, most of them can easily be set to nominal values and have a minimal effect on the global functioning of the controller. Hence, the tuning effort can be focused to a single parameter. In addition, using ad-hoc stringent assumption of linear dynamics, a stability condition is derived, which can serve as an indicative target range for the experimentalist. The method is then tested both on numerical examples, Section 3, and experimental test rigs including a variety of nonlinear forces, Section 4. In each of the reported cases, the NCPLL shows its ability in achieving fast measurements while minimizing the tuning effort. Concluding remarks are given in Section 5.

2 Phase-Locked Loop (PLL)

The Phase-Locked Loop is frequently used in electronics and communications for synchronizing two signals both in frequency and phase, see *e.g.* [3,18] and references therein. Its widespread applications include for

instance: signal demodulation in communication systems, frequency synthesis, clock data recovery, storage systems control, harmonic compensation and motor control [3]. Applications to experimental continuation in the field of mechanical vibrations started in the 2010s [28,33]. This section briefly recalls the typical design used nowadays in such a control loop, and then introduces the nonlinear controller, proposed for improving the general functioning.

2.1 Conventional Phase-Locked Loop for mechanical system identification

The general architecture of a PLL for experimental continuation of mechanical systems is summarized in Fig. 2.1. The main components of a conventional PLL are listed as: (i) a phase detector, which is needed to decompose the signal and extract the phase of the intended harmonic; (ii) a proportional-integral PI-controller to adjust the excitation frequency from the error between the target phase lag and the estimated phase difference between the excitation and the response; (iii) a Voltage Controlled Oscillator (VCO) which generates the excitation voltage sent to the amplifier-exciter assembly. The choice of the phase detector has evolved from the first PLL proposals to the most recent ones. While Least Squares harmonics fit (LSF) has been used in early stages [48], synchronous demodulation [8] and Least-Mean Square (LMS) adaptive filtering [2] are now more commonly used. In this contribution, LMS adaptive filtering is selected for phase detection, following the results shown in [17] which underline a general better performance as compared to other settings.

Due to the presence of noise, higher and sub-harmonics, the phase estimation is never perfect, but can be within a given error tolerance. Therefore, the number of harmonics considered affects the accuracy of the phase detection. Importantly, the phase detector must be fast enough to avoid destabilizing the whole system [8]. As shown in Fig. 2.1, the PLL coupled to the exciter and structure form an auto-resonant system which is easier for phase-control with the advantage of stabilizing resonant regimes because of the flatness and single-valuedness of the amplitude-phase relation [45] for well separated modes.

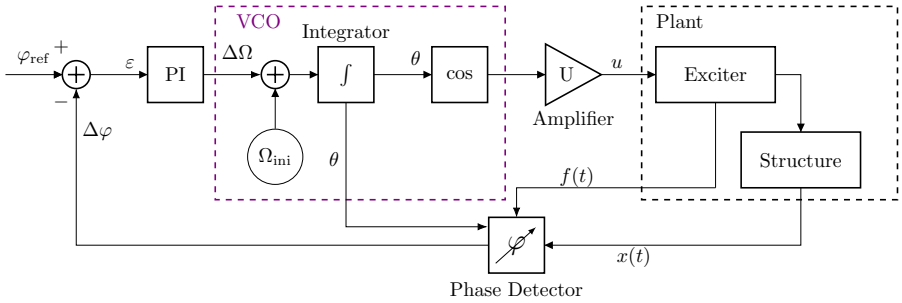

Fig. 2.1: Conventional PLL architecture, where the internal features of the Voltage-controlled oscillator (VCO) have been highlighted in the dashed purple box.

In nonlinear vibrations, the experimentalist is generally interested in having access to both the backbone curve of the different modes, which informs about the amplitude-frequency dependence; and the Frequency-Response Curve (FRC), which shows maximal vibration amplitudes and bifurcations. The backbone curve can be attained in a PLL experiment by setting the targeted phase lag as $\varphi_{\text{ref}} = \pi/2$. With this choice, the PLL fulfills the phase quadrature criterion automatically and can track the backbone for increasing amplitudes [33]. To obtain an FRC, the phase lag can be set as variable in order to cover a whole interval ($\varphi = [0,\ \pi]$). The phase error ε is defined as the difference between the measured phase lag $\Delta\varphi$, output from the phase detector, and the prescribed phase reference φ_{ref}

$$\varepsilon = \varphi_{\text{ref}} - \Delta\varphi. \tag{2.1}$$

As shown in Fig. 2.1, the phase error is then corrected by the PI-controller. Hence, an accurate setting of the controller gains is a crucial step for the performance of the technique. Unfortunately, since no general tuning rule exists at present and might depend upon the nonlinearity of the measured system, the setting is generally done by trial and error.

Summarizing the main components of a conventional PLL, it appears that 6 parameters are to be adjusted: PI-controller gains, k_p and k_i, LMS adaptive filter cutoff frequency, ω_{c}, sampling time, T_{s}, number of harmonics, H and initial frequency, Ω_{ini}.

The setting for the initial frequency is generally taken as $\Omega_{\text{ini}} = \omega_0$, where ω_0 is the underlying natural frequency identified at low excitation amplitude. This is done to improve the convergence of the algorithm around the targeted mode. The sampling time is fixed by the acquisition frequency of the experimental set-up. The number of harmonics H is recommended to be selected as high as possible, however for practical reason this number cannot be too large to avoid long computation time.

A practical recommendation for the selection of the LMS adaptive filter cut-off frequency is detailed in [17], which is adopted herein. The tuning of the PI-controller gains is mostly heuristic since no general rule has been provided yet that can be used for all cases. The experimentalist is thus led by case-by-case studies and his own experience. However in [17], a systematic approach to selecting the controller gains is proposed. Nevertheless, to the best of our knowledge, such approach was only validated for a system with nonlinear stiffness.

2.2 Nonlinear-Controller Phase-Locked Loop (NCPLL)

In order to reduce the test duration as well as the number of parameters to be defined, the linear PI-controller is replaced by a nonlinear controller, following the early proposal given in [41], giving rise to a Nonlinear-Controller Phase-Locked Loop (NCPLL). The stability analysis is performed, elaborating on the assumptions used in [17]. The main result is that the tuning effort can be focused to a single parameter: the nonlinear controller gain. Setting the other parameters to nominal values is found to be sufficient and leads to a robust design. A condition on the nonlinear controller gain is investigated analytically from stability analysis of the underlying linear dynamics. Since the stability condition is only indicative, for reasons detailed later in the text, it is provided in Appendix 1. Nonetheless, this indicative value remains useful for experimentalists, offering a practical guideline for tuning the controller - as further discussed in the numerical and experimental results.

The NCPLL design is shown in Fig. 2.2.Two additional components are added to the controller branch of the PLL: a nonlinear element and a first order low-pass filter. The low-pass filter serves to slow down the controller with respect to the phase detector, which is a notable advantage since being a necessary condition for faster phase estimation [8].

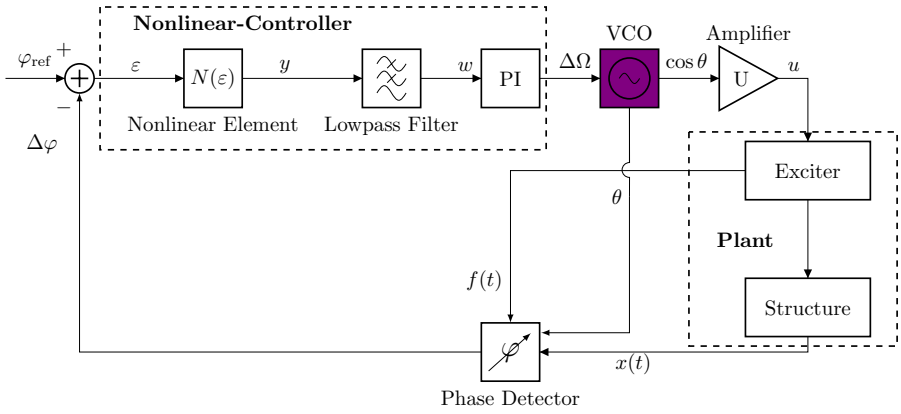

Fig. 2.2: NCPLL architecture: A nonlinear element and a first-order filter are added to the controller branch of the PLL to enhance the convergence speed of the algorithm.

Following [41], the nonlinear element is selected as an hyperbolic tangent function, N of the error, as defined in Eq. (2.2),

$$y = N(\varepsilon) = K_{\text{n}} \tanh\left(\frac{\varepsilon}{\beta}\right), \tag{2.2}$$

where $K_{\text{n}} > 0$ is the gain, and $0 < \beta < 1$ is the steepness parameter. Note also that a close idea is inspected in [11], where the signum function is inserted in the loop. To suppress the high frequency components of y, a low-pass filter with transfer function,

$$L(s) = \frac{1}{s/\alpha + 1}, \tag{2.3}$$

is added to the nonlinear component; where α is the cut-off frequency (not to be confused with the cut-off frequency of the phase detector), and s the Laplace variable. The effect of the steepness parameter in Eq. (2.2) is illustrated in Fig. 2.3. As shown, decreasing β implies faster convergence, but too small value can cause non-smooth transition. The value of β is not system-dependent and can be fixed once and for all. Herein, we choose $\beta = 0.1$ because it gives an excellent compromise between fast convergence and smooth transition as recommended in [41]. To further justify this choice in the framework of nonlinear vibrations, the effect of β is investigated in Section 3.1 involving numerical simulations with a Duffing oscillator. It will be shown on this specific example that when a too small value is selected for β, then the transients are longer, making the steady states more difficult to reach. On the other hand, large β values lead to longer convergence. The nonlinear element ensures that the control output is bounded by K_{n}, hence, avoiding large overshoots.

The addition of the nonlinear element and low-pass filter, introduces three additional degrees of freedom, K_{n}, α and β. Retaining the above approach for selecting the parameters, T_{s}, ω_c, H, Ω_{ini} and β, the PI-controller gains, k_p and k_i can be set to unity in order to focus the tuning effort on the nonlinear gain K_{n}, thus, eliminating the control demand on them. The low-pass filter cut-off frequency, α can be chosen following the recommendation outlined in Section 2.3. Thus, only one parameter remains to be tuned: K_{n}.

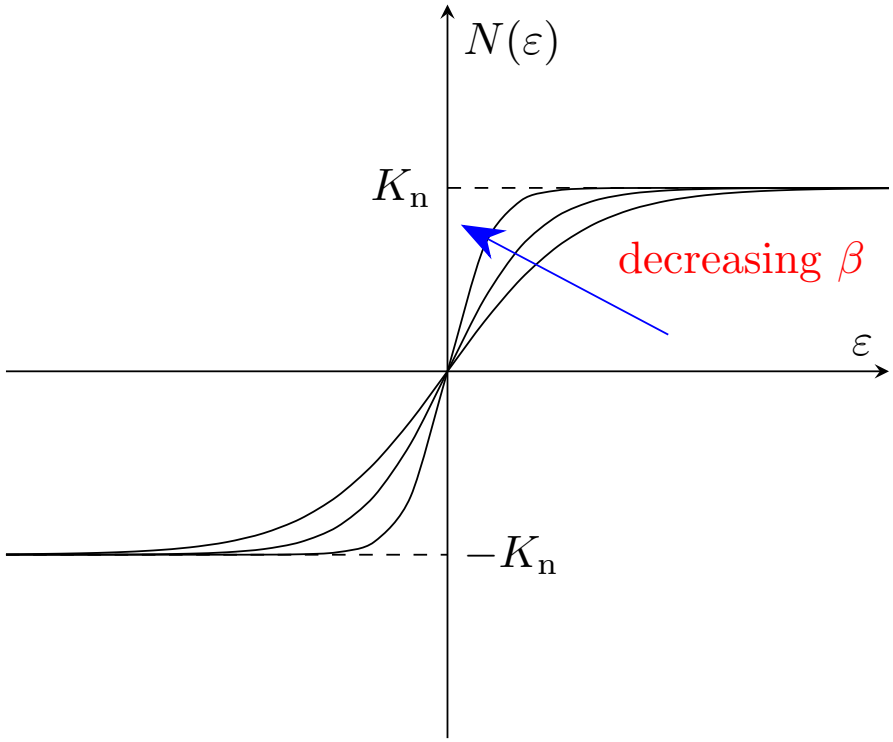

Fig. 2.3: Effect of the steepness parameter, β. Decreasing β implies faster convergence but a too small value can introduce sharp transitions which can be undesirable.

2.3 Stability analysis of the closed loop system

In this section, the dynamics of the closed loop system is studied. A linear stability analysis is reported in Appendix 1. Based on this analysis and the discussion on the validity of such analytical bounds - derived in the context of PLL and reported in [11] - practical guidelines are provided to the experimentalist for achieving a rapid yet effective tuning of the controller. and , which allows proposing a simple tuning rule for this parameter. The analysis of the closed loop system strictly follows the one reported in [17]. In particular, the same modeling assumptions as in [17] are here endorsed: linear vibrations are assumed, the dynamics of the exciter is taken into account and the inductance of the coil is neglected. The only difference with [17] lies in the consideration of the nonlinear controller in the loop. The variables needed to describe the closed loop system shown in Fig. 2.1 are: the output voltage from the amplifier u, the excitation frequency Ω, the phase error ε already defined in Eq. (2.1), the voltage y output from the nonlinear controller and w from the low-pass filter. I_w is an auxiliary term. All in all, the equations describing the system read:

$$
\begin{aligned}
u &= U\cos(\theta), && (2.4)\\
\theta &= \int_0^t \Omega \mathrm{d}\tau, && (2.5)\\
\Omega &= \Omega_{\mathrm{ini}} + w + I_w, && (2.6)\\
\varepsilon &= \varphi_{ref} - (\hat{\varphi}_f - \hat{\varphi}), && (2.7)\\
y &= K_{\mathrm{n}} \tanh\left(\frac{\varepsilon}{\beta}\right), && (2.8)\\
\dot{\bar{w}} &= -\bar{\alpha} w + \bar{\alpha} y && (2.9)\\
\dot{\bar{I}}_w &= w, && (2.10)\\
\hat{\varphi}_f &= \mathrm{Arg}\left\{\hat{F}^{(1)}\right\}, && (2.11)\\
\hat{\varphi} &= \mathrm{Arg}\left\{\hat{Q}^{(1)}\right\}. && (2.12)
\end{aligned}
$$

Note that Eq. (2.8) - Eq. (2.10) come from the nonlinear element and its low-pass filter, and are thus the main difference with the derivation provided in [17]. Also, the proportional and integral gains of the PI-controller are here set to unity. Eq. (2.10) is an auxiliary equation. A normalized time $\bar{t} = \omega_c t$ is introduced, so that $\bar{I}_w = \omega_c I_w$, and $\bar{\alpha} = \dfrac{\alpha}{\omega_c}$. A complete derivation and study of this system is provided in 1. In particular, the harmonic decomposition for force and response, retaining only the fundamental harmonic terms, $\hat{F}^{(1)}$ and $\hat{Q}^{(1)}$ appearing in Eq. (2.11)-Eq. (2.12) are given. The stability analysis is about the resonance phase reference ($\varphi_{\mathrm{ref}} = \dfrac{\pi}{2}$), thus the gain obtained herein is optimized for the resonant regime and may differ for other responses.

The complete study of the closed loop system is reported in Appendix 1. The results show that $K_{\mathrm{n}} > 0$ is a sufficient stability condition. It yields an upper bound which is found to however, depend on $\bar{\alpha}$, the normalized cut-off frequency of the low-pass filter. Moreover, in the limit of large $\bar{\alpha}$, the upper bound tends to infinity. This is a practical limitation as one does not expect an infinite gain, and large gains can drive the system away from the stable point. As noted in [11], such analytical bounds may be inconsistent with what is observed numerically, principally due to errors in the frequency tracking coupled with computational errors. Due to large gains, the system's transient dynamics may exhibit overshoots, potentially leading to instability even when the system is analytically predicted to be stable. For all these reasons, the analytical predictions may only be used as a guideline for practical tuning. From our experience, we suggest to set $K_{\mathrm{n}} = 1$, which will generally drive the system to convergence. However, the presence of nonlinearity may require a higher gain and for this reason, we recommend the use of Eq. (1.70) as a starting point. As noise can introduce significant oscillations about the target, or large oscillations are observed due to K_{n} being large, it is then possible to tune down the gain until these oscillations die out.

2.4 Procedure for the NCPLL

A summary of the experimental procedure for setting up the NCPLL is now provided. Supposing that the linear modal data have been extracted, following for example the method outlined in [17], the parameters for the NCPLL are then derived as below.

Selecting the Parameters for the NCPLL The NCPLL set-up includes five parameters that have to be selected by the experimentalist: the number of harmonics H, the adaptive filter cut-off frequency ω_c, and the nonlinear element parameters, β, α and K_{n}. For practical applications, β can be set to $\beta = 0.1\,\mathrm{rad}$ as already explained in Section 2.2. This reduces the number of independent parameters to four. The choice of ω_c and H can be governed by the method outlined in [17], that is by open loop testing for cut-off frequencies between the range $1/100 < \omega_c/\omega_0 < 1$, where ω_0 is the underlying linear system natural frequency, and selecting the largest value that respects the error tolerance. This strategy has been found effective in giving a fast tuning for this parameter.

The cut-off frequency α of the nonlinear controller low-pass filter, Eq. (2.3) is normalized by the adaptive filter cut-off frequency, ω_c in Eq. (1.55), where $\bar{\alpha}$ is taken as a positive integer.

K_{n} is linearly proportional to $\bar{\alpha}$ as shown in Fig. 1.2. From our experience, a value in the range $1 < \bar{\alpha} < 100$ is recommended. Finally, only one parameter K_{n} is to be tuned. It should be noted that the experimentalist choice of $\bar{\alpha}$ will be directly transferred to K_{n}, thus only the tuning of K_{n} is necessary. That is, while there are more parameters in the NCPLL design, the burden of control is concentrated on one parameter only.

Lock-in detection and Algorithm for backbone tracking Let us finally describe the handling of lock-in and voltage transition levels, for the specific case of a backbone tracking. Note that this choice is not restrictive

and the same procedure applies for the measurement of an FRC. One has simply to change the targeted phase shifts as already explained in Section 2.

Hippold *et al.* recommended half-cosine ramps to ensure smoother transition between voltage levels during the backbone tracking [17]. However, it is clear that such a choice importantly increases the testing time as compared to the case of step increase. Due to the robustness of the NCPLL to sudden change, stepwise variations in the supplied voltage are manageable, which is a supplementary advantage of using a nonlinear controller. Consequently, the voltage $\boldsymbol{U}$ is defined as a vector, ranging from U_0 to $U_{\max}$, with a step ΔU: $\boldsymbol{U} = [U_0 : \Delta U : U_{\max}]$..

A state is considered as locked if the phase lag is continuously below the specified tolerance, $|\varepsilon| \leq \varepsilon_{\text{tol}}$. This is ensured by recording N samples such that the error tends to zero. If this condition is satisfied, the average is taken and recorded, then the counter is set back to 0, and the voltage amplitude incremented. The process is summarized in Algorithm 1.

Algorithm 1: NCPLL: Algorithm for backbone curve tracking.

```
N Number of successive samples required;
n Counter: Number of successive samples;
Input: |ε|, ε_tol, N
Output: U
initialization: U(1) = U_0, n = 0;
if (|ε| ≤ ε_tol & n ≥ N) then
    U(i) = U(i − 1) + ΔU;
    Reset n;
    Repeat process until U_max;
    Then Stop Simulation
end
```

A similar algorithm can be adapted for the tracking of the frequency response curve. In this case the forcing amplitude is prescribed and a stepped-phase sweep, $\varphi_{ref} = 0$ to $\varphi_{ref} = \pi$ is performed. Thus, in Algorithm 1, $\boldsymbol{U}$ is replaced by the vector of phase targets. Due to exciter structure interaction, it is important to maintain constant forcing of the structure and this can be ensured by amplitude control using a simple PI-controller as illustrated in Ref. [34].

3 Numerical validation

This section is devoted to demonstrate the effectiveness of the NCPLL for extracting backbone curves and FRCs of typical nonlinear oscillators through numerical experiments. Four cases are treated, including a Duffing oscillator, friction-damped oscillator, a friction damped oscillator with cubic and quintic stiffness, and a finite element beam model.

For all the numerical simulations shown hereafter, the NCPLL parameters have been set as follows. The phase detector is the LMS adaptive filtering and the number of harmonics H selected is such that $H = 10$. The gains k_p and k_i are set to unity as recommended before such that no tuning is needed for them. The linear frequency f_0 of the simulated oscillators have been set to $f_0 = 62.8$ Hz, and a small damping ratio has been selected as ζ =0.05%. Backbone curves are computed by setting the target phase to $\pi/2$ while increasing the amplitude of excitation, and FRCs are obtained by imposing a phase sweep between 0 and π radians at constant forcing. In such a case, the initial external excitation frequency Ω is started from the value $\Omega_{\text{ini}} = \omega_0$. The phase detector cut-off frequency is selected as $\omega_{\text{c}} = \omega_0/3$, and the two main parameters to be set for the NCPLL have been set once and for all based on the linear characteristics. The low-pass filter cut-off parameter $\bar{\alpha}$ has been set as $\bar{\alpha} = 30$. Finally, the gain K_{n}, following Eq. (1.70), is set as $K_{\text{n}} = 5.919$, and found to stabilize all the orbits at resonance and away from resonance. Suggesting that we are well within the stability region with this parameter combination. All the simulations have been carried out with the Dormand-Prince formula for the Runge-Kutta numerical integrator, with the version `ode45` implemented in Matlab/Simulink.

3.1 Duffing oscillator

The Duffing oscillator is described in Eq. (3.1).

$$\ddot{q} + 2\xi\omega_0\dot{q} + \omega_0^2 q + \Gamma^{(3)} q^3 = F\cos\theta. \tag{3.1}$$

with θ as defined in Eq. (2.5).

The linear characteristics have been set as explained in the previous section. The cubic parameter is selected as $\Gamma^{(3)} = 5 \times 10^5 \text{Nm}^{-3}$.

The effect of β is first investigated with this example. Fig. 3.1 clearly shows that with a too small value $\beta < 0.05$ the transients will take longer to decay and too large a value will delay convergence. It is shown that $\beta = 0.1$ gives an excellent compromise between time for transient decay and time of convergence, as recommended in [41].

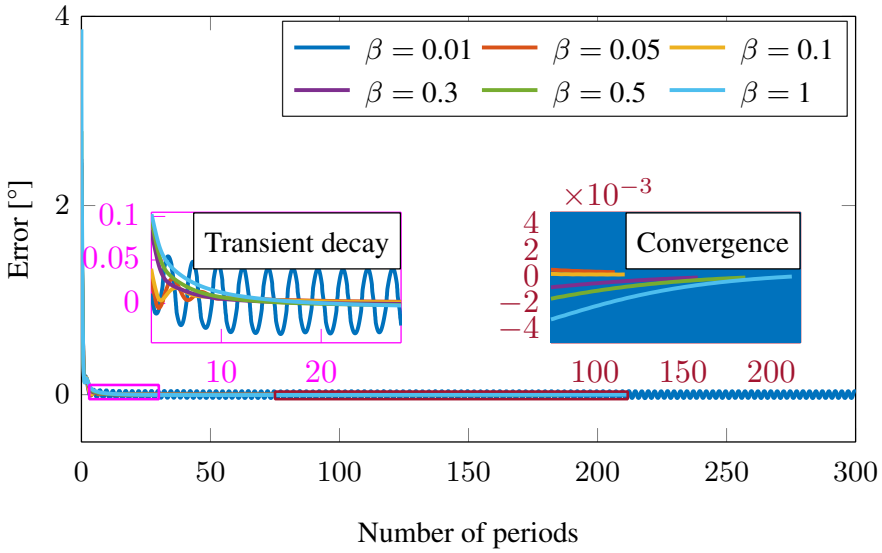

Fig. 3.1: Effect of β: Compromise between time for transient decay and convergence to the specified tolerance.

Fig. 3.2 shows the backbone curve obtained with the NCPLL algorithm together with three FRCs obtained for increasing levels of forcing: $F = 1, 5, 10$ N. To draw out a comparison with the exact solution, the same nonlinear characteristics are computed with a numerical continuation method, taken as reference. To that purpose, the Asymptotic-Numerical Method (ANM) implemented from a harmonic balance solution in the software Manlab [6,15,16], has been used. The proposed design of the NCPLL accurately extracts the hardening characteristics of the Duffing oscillator, and the backbone curve corresponds well to the peak of the frequency response curves. Importantly, the NCPLL stabilizes all orbits with the calculated control parameter, K_{n}, no extra tuning being required. It took about 10 s in real time to track the backbone curve (for a total number of 100 computed points) with excellent accuracy and minor oscillations. This highlights the strength of the NCPLL in accurately extracting the nonlinear characteristics within a short duration.

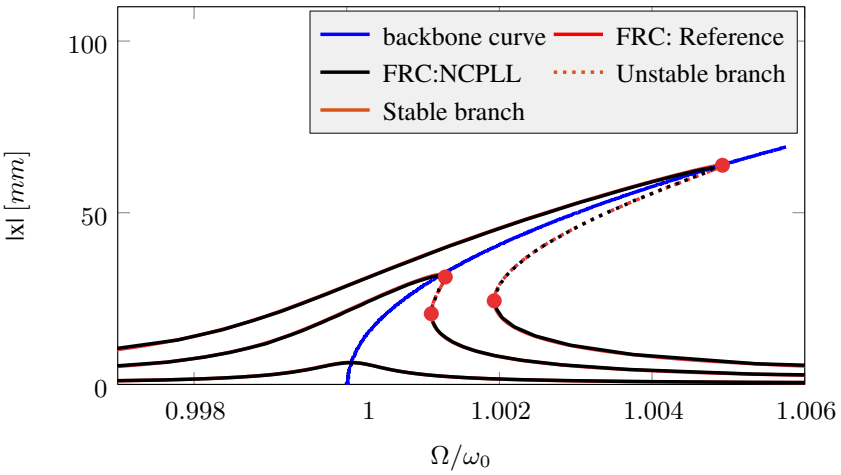

Fig. 3.2: Backbone curve (solid blue line) and frequency response curves for the Duffing oscillator. Results obtained with NCPLL (in black) are compared to a reference solution (numerical continuation, harmonic balance with asymptotic-numerical method, in red). $\Gamma^{(3)} = 5 \times 10^5 \mathrm{Nm}^{-3}$. FRC for increasing levels of forcing amplitude: $F = 1, 5, 10$ N, Backbone curve: $F = 0.01$ to $F = 11$ N with step $\Delta F = 0.01$ N.

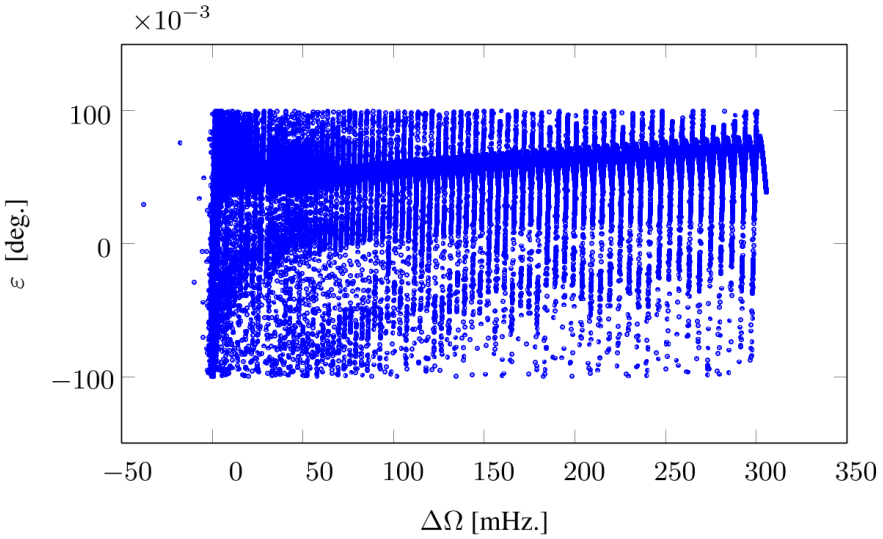

Fig. 3.3: Frequency incertitude along the backbone curve.

The locked state is defined by the fulfillment of the phase target below the specified error tolerance. The frequency may fluctuate about this state. Though not often reported in the literature, we provide insight into the issue. Fig. 3.3 shows the frequency fluctuation and convergence at different points on the backbone curve. In this figure, the abscissa shows the increment in terms of excitation frequency $\Delta\Omega$ when travelling along the backbone curve shown in Fig. 3.2. The first points correspond to the initiation of the computation of the backbone curve at low energy (linear range), while the maximum value reached correspond to the upper point of the backbone curve. Note that the points in the range $\Delta\Omega[-50, 0]$ mHz correspond to the initialization effect of the solver (here, the initial condition of the integrator is 0), and has been included for completeness. Therefore, $\Delta\Omega = 0$ simply corresponds to the purely linear response, that is no frequency change from ω_0. At lower energy levels, the points do not align perfectly, but are clustered around acceptable value, indicating some oscillations. As energy increases, the certainty is improved and the points align indicating less oscillations at these levels and an improved functioning of the tracking algorithm. In all the cases, the certainty lies within acceptable values. This observation is important for experiments as one need to ensure near constant excitation frequency to isolate a mode.

The parameter values for the Duffing oscillator has been selected following those reported in [8]. Interestingly, a conventional PLL can be run on the same example, where the gains are set as proposed in [8], *i.e.*: $k_\mathrm{p} = 0.5\ s^{-1}$ and $k_\mathrm{i} = 10\ s^{-2}$. Results are reported in Fig. 3.4, highlighting that without a proper tuning of the PLL parameters or longer settling time (which are not reported in [8]), the method encounters extreme difficulties in converging to the exact periodic orbits of the original system. This example underlines that conventional PLL schemes necessitate additional tuning rules that are generally not made explicit in the literature. On the other hand, the NCPLL does not ask for further tuning and the nonlinear controller allows converging easily and rapidly to the correct solution. Additional comparisons for this specific example of the Duffing oscillator are presented in 2 to draw out a more complete illustration of the gain in using NCPLL as compared to a classical PLL with linear controller. The results of the conventional PLL can be made much better with proper tuning, but also with longer test duration time. However, this is not recommended since the goal is to speed up the experimental tests. For this reason, the comparison in 2 highlights the need for a robust control for accurate measurements.

Even in the presence of noise, NCPLL shows remarkable potential in keeping the error minimal. White noise was added to the excitation signal and the signal-to-noise ratio (SNR) varied between 5 and 40. In Fig. 3.5, as the SNR worsens, the maximum phase error is about 2°, showing that even in such adverse condition, the NCPLL keeps the phase error within acceptable range. In real time application, the presence of noise can cause oscillations about the specified tolerance with the calculated gain, K_n. It is then possible to gradually reduce the gain until the oscillations die out, and the error tolerance is reached.

In the next selected examples, the capability of the NCPLL is further examined numerically on systems with other nonlinearity types. For these cases, no numerical references are given.

3.2 Oscillator with Coulomb friction

The case of a linear oscillator with Coulomb friction is now considered. The equations of motion read:

$$\ddot{q} + 2\xi\omega_0\dot{q} + \omega_0^2 q + f_\mathrm{R} \quad = \quad F\cos\theta, \tag{3.2}$$

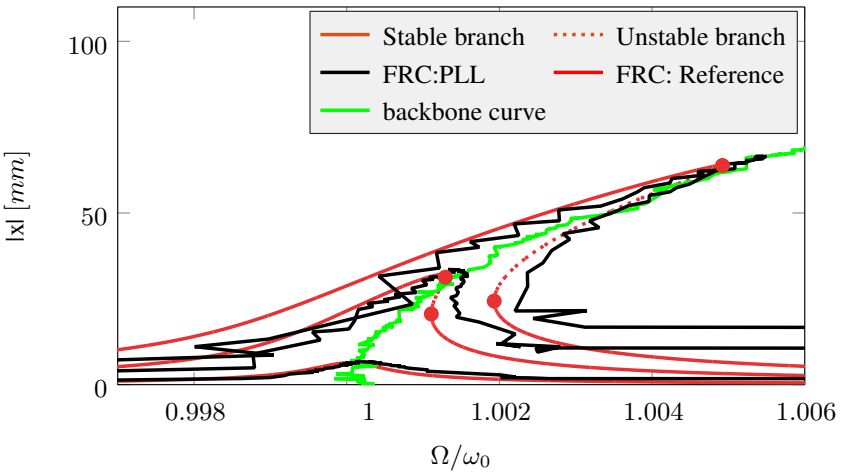

Fig. 3.4: Backbone and frequency response curves for the Duffing oscillator. Numerical results obtained with standard PLL algorithm compared to numerical continuation technique as reference. $\Gamma^{(3)} = 5 \times 10^5 \mathrm{Nm}^{-3}$. Parameters for the PLL taken as: $k_\mathrm{p} = 0.5\ \mathrm{s}^{-1}$, and $k_\mathrm{i} = 10\ \mathrm{s}^{-2}$. FRC for increasing levels of forcing amplitude: $F = 1, 5, 10$ N, Backbone curve: $F = 0.01$ to $F = 11$ N with step $\Delta F = 0.01$ N.

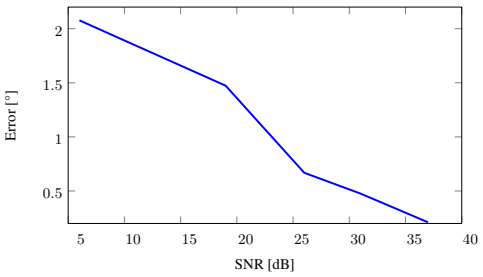

(a) Error variation with noise level.

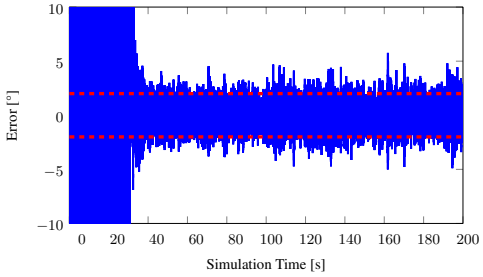

(b) Error convergence ($SNR = 5\ dB$).

Fig. 3.5: Robustness to noise (Red dashed line is $\pm 2°$). NCPLL shows excellent handling of noisy signals.

where the linear characteristics are left unchanged as compared to the previous Section. The nonlinear force f_R consists of a linear spring connected to a non-smooth Coulomb friction, following the models presented *e.g.* in [22,21]. The nonlinear restoring force, expressed in differential form, writes:

$$\mathrm{d}f_\mathrm{R} = \begin{cases} \omega_\mathrm{t}^2 q & \text{if} \quad |f_\mathrm{R} + \omega_\mathrm{t} \mathrm{d}q| < \nu N \quad \text{(stick)}, \\ 0 & \text{if} \quad |f_\mathrm{R} + \omega_\mathrm{t} \mathrm{d}q| \geq \nu N \quad \text{(slip)} \end{cases} \tag{3.3}$$

In this expression, ω_t^2 represents the squared radian frequency associated to the linear contact stiffness, and νN the limit friction force, where N is the normal force. Note that such differential expression is equivalent to the classical Coulomb friction law expressed on the velocity, where the mass of the sliding element has been neglected [25]. For the numerical simulations, the parameter ν has been set such that the tangential force $\nu N = 1$, and the linear stiffness has been set to $\omega_\mathrm{t} = 800\,\mathrm{rad/s}$. Eq. (3.3) has been resolved using the stick-slip switch algorithm proposed in [26], with the regularization parameter set to 0.1.

The solution branches are computed for the unforced case (backbone curve), and three FRCs are reported for increasing values of the forcing amplitude F. The results are shown in Fig. 3.6, where the frequency axis has been normalized by the eigenfrequency ω_0. Following the results presented for example in [22,21], for small amplitudes of vibrations, sticking occurs such that the system behaves equivalently to a linear oscillator where the stiffness is conveyed by both the linear restoring force and the contact stiffness k_t. This value is referred to as the linear eigenfrequency with sticking, and exactly corresponds in the present case, with the selected values to $\Omega/\omega_0 = 1.0026$. For larger amplitudes, sliding occurs and the system experiences a softening behaviour. Finally, for large amplitudes, the equivalent stiffness of the friction element tends to zero [22,21], consequently the backbone curve with the present normalization tends to 1.

The NCPLL algorithm shows a remarkable behaviour in this case of friction-damped oscillator and effectively retrieves all the awaited characteristics. Without extra tuning and using the same control parameters for both cases, the NCPLL correctly stabilizes all orbits and has been able to follow both the backbone curve and FRCs with increasing amplitudes.

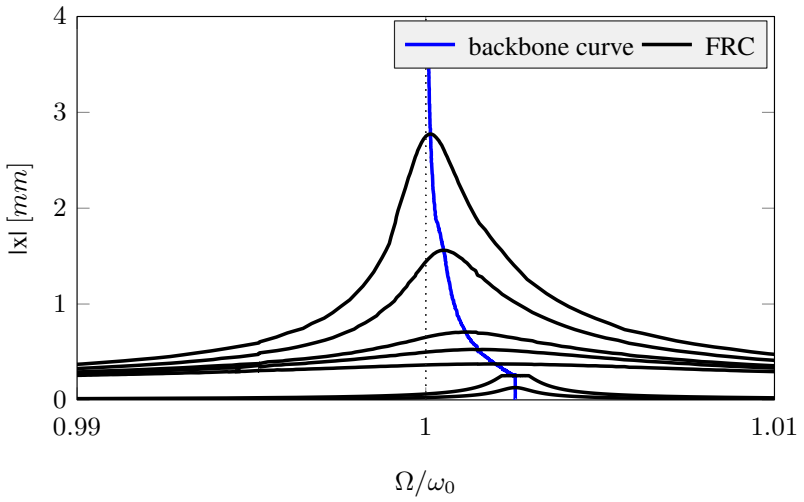

Fig. 3.6: Backbone and frequency response curves for the Coulomb oscillator. $\nu N = 1$. FRC: $F = 0.02$, 0.05, 0.5, 1, 1.2, 1.5, 1.75 N, Backbone curve: $F = 10^{-4}$ to $F = 1.8$ N with step $\Delta F = 0.0018$ N. Dashed line shows the natural frequency.

3.3 An oscillator with friction, cubic and quintic stiffness

A third oscillator example is selected which combines smooth and non-smooth (friction) nonlinearities. The equations of motion reads:

$$\ddot{q} + 2\xi\omega_0\dot{q} + \omega_0^2 q + \Gamma^{(3)}q^3 - \Gamma^{(5)}q^5 + f_{\mathrm{R}} \quad = \quad F\cos\theta. \tag{3.4}$$

In that case, the Coulomb friction law as given by Eq. (3.3) with $\nu N = 1$ is selected, the smooth cubic and quintic nonlinear terms are set as $\Gamma^{(3)} = 5\times10^{8}\mathrm{Nm}^{-3}$ and $\Gamma^{(5)} = 5\times10^{13}\mathrm{Nm}^{-5}$, while the linear characteristics are left unchanged. This case is selected to test the NCPLL in a case where hardening and softening behaviours alternate.

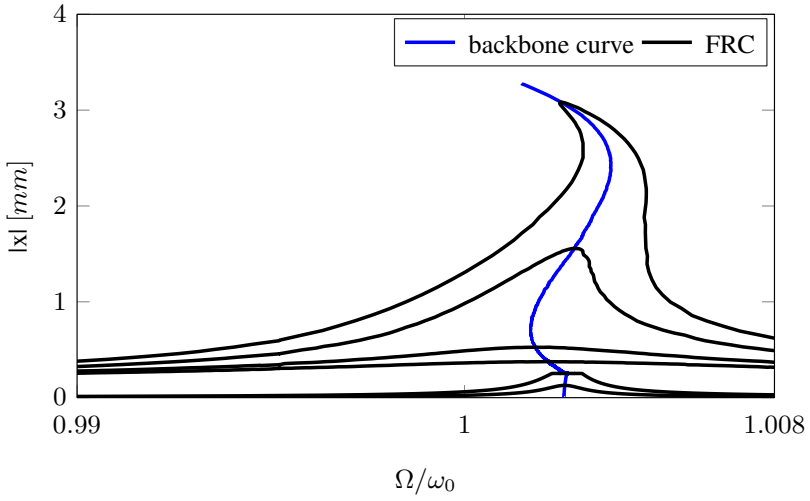

Fig. 3.7: Backbone and frequency response curves for the oscillator with cubic and quintic nonlinearities with opposite signs. $\nu N = 1$, $\Gamma^{(3)} = 5\times10^{8}\mathrm{Nm}^{-3}$, $\Gamma^{(5)} = 5\times10^{13}\mathrm{Nm}^{-5}$. FRC: $F = 0.02$, 0.05, 1, 1.2, 1.5, 1.75 N, Backbone curve: $F = 10^{-4}$ to $F = 1.8$ N with step $\Delta F = 0.0018$ N.

Results for both the backbones and FRCs are displayed in Fig. 3.7, showing the ability of the NCPLL to extract the nonlinear characteristics with varying dominant nonlinear phenomenon at certain amplitudes. For very small amplitudes, linear behaviour is observed then, a softening characteristic due to dry friction, followed by hardening as amplitude is increased. Beyond a certain amplitude, the negative quintic coefficients starts to dominate and a softening trend is at hand. This example underlines the versatility of the NCPLL to deal with

different nonlinear behaviours. Importantly, no extra parameter tuning is required. All the simulations reported in Fig. 3.7 have been realized with a single value of the gain $K_n = 5.919$ with fast convergence.

3.4 A finite element beam with localized nonlinearities

The last numerical example is devoted to a finite element (FE) cantilever beam model which has again combined localized nonlinearities. The FE model, shown in Fig. 3.8a is composed of ten linear beam elements with two degrees-of-freedom at each node (bending and torsion). Localized nonlinearities are added at two different points of the beam: a nonlinear cubic stiffness is inserted at node point 2, with cubic parameter set as $k_{\mathrm{nl}} = 5{\times}10^5 \mathrm{Nm}^{-3}$; and a linear stiffness and a friction Coulomb damping is considered at node point 3, with parameters set as $\nu N = 1$, $k_{\mathrm{t}} = 8 \times 10^5 \mathrm{N/m}$. The external forcing is set at point 2, and a complete exciter model, following [38], is implemented. Experimental continuation in the vicinity of the second bending mode is investigated, which has an eigenfrequency f_2 equal to $f_2 = 21\,\mathrm{Hz}$.

Table 3.1 summarizes the control parameters adopted for this case. Numerical integration is here performed with the Rosenbrock scheme, as implemented in the matlab function `ode23s`. Note that as compared to the three previous oscillator examples, which used the exact same linear characteristics, the eigenfrequency of the second flexural mode and its damping ratio (respectively $\omega_2 = 132.25 rad/s$ and $\zeta_2 = 0.05\%$) have here different values. Consequently the control parameters have been recomputed to fit that case, leading in particular to a value for the gain set as $K_n = 1.3228$.

Table 3.1: Control parameters for the FE beam simulation.

Parameter set	Phase detector	f[Hz]	ζ[%]	Ω_{ini}	$\omega_{\mathrm{c}}/\omega_0$	$k_{\mathrm{p}}[\mathrm{s}^{-1}]$	$k_{\mathrm{i}}[\mathrm{s}^{-2}]$	$\bar{\alpha}$	K_{n}
NCPLL	$H = 10$	21	0.05	$\omega_0/1.5$	0.1	1 (fixed)	1 (fixed)	20.0	1.3228

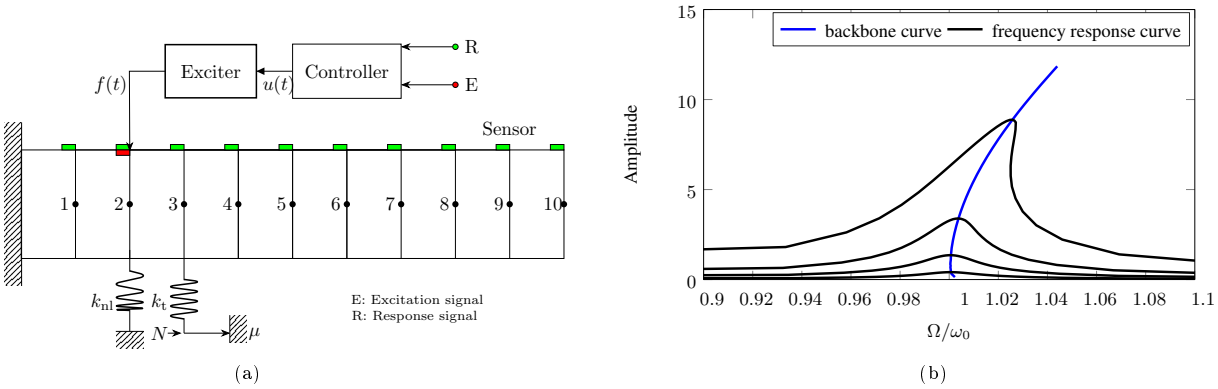

Fig. 3.8: (a) FE model of a cantilever beam with localized nonlinearities: cubic stiffness and excitation at node 2, localized linear stiffness and friction at node 3. (b) Backbone curve and FRCs in the vicinity of the second bending mode obtained by NCPLL.

Fig. 3.8b shows the results provided by applying the NCPLL experimental continuation to that case. Regarding the backbone curve, one can clearly observe that the softening trend for small amplitudes, due to the friction nonlinearity, is then dominated by the hardening nonlinearity due to the cubic nonlinear restoring force, for larger vibration amplitudes. Three FRCs have also been computed, for increasing values of the forcing selected as $F = 0.1, 0.5, 1, 2$ N. For both cases, the NCPLL demonstrated its ability in identifying the nonlinear behaviour of the second mode of the beam with excellent accuracy. For this example, the exciter model in [38] was implemented causing the model to be very stiff, thus the simulation time is considerably long (about 15 minutes in real time on a standard PC with 13th Gen Intel CPU -Corei5-1345U). However, 30 periods were needed for a response point in average which corresponds to about 136 s in simulation time.

The above numerical examples have demonstrated the robustness of NCPLL to different nonlinearities, and the ease of tuning which eliminates the conventional trial and error approach consequently improving testing duration. In the above numerical studies, the choice of $\bar{\alpha}$ was not governed by any criterion, and the contribution of the low-pass filter is not evident since the cut-off frequency is higher than the cut-off frequency of the phase detector. One might consider removing the low-pass filter in the NCPLL loop. However, it proves necessary

in conditions where noise level is significant. Experimental results are presented next to validate the proposed method.

4 Experimental validation

Two different examples have been selected in order to demonstrate the effectiveness of the NCPLL in real life experiments. The first one considers a smooth nonlinearity created by a magnetic field. The second example consists of assembled beams bolted with joints.

4.1 Piezomagnetoelastic cantilever beam

The experimental set-up, shown in Fig. 4.1, consists of a cantilever beam made of steel. The beam is hanged at its top clamped end, while the free end is oscillating in the magnetic field created by two permanent magnets. Two piezoelectric patches are glued on both side of the beam, near the clamped end, and are used for actuation. Such a set-up has been historically used in order to evidence the existence of chaotic vibrations [29,47], and is also used for the purpose of energy harvesting [19]. Importantly, the vibration of a cantilever beam in the magnetic field of two permanent magnets has been investigated in [47,19], such that approximate nonlinear models are available in order to have an understanding of the involved nonlinearities. Depending on the relative position of the magnets and the beam, the system can have one or two stable equilibria, and the restoring force from the magnetic fields can be approximated with a combination of linear, cubic and quintic stiffness [47,19,5].

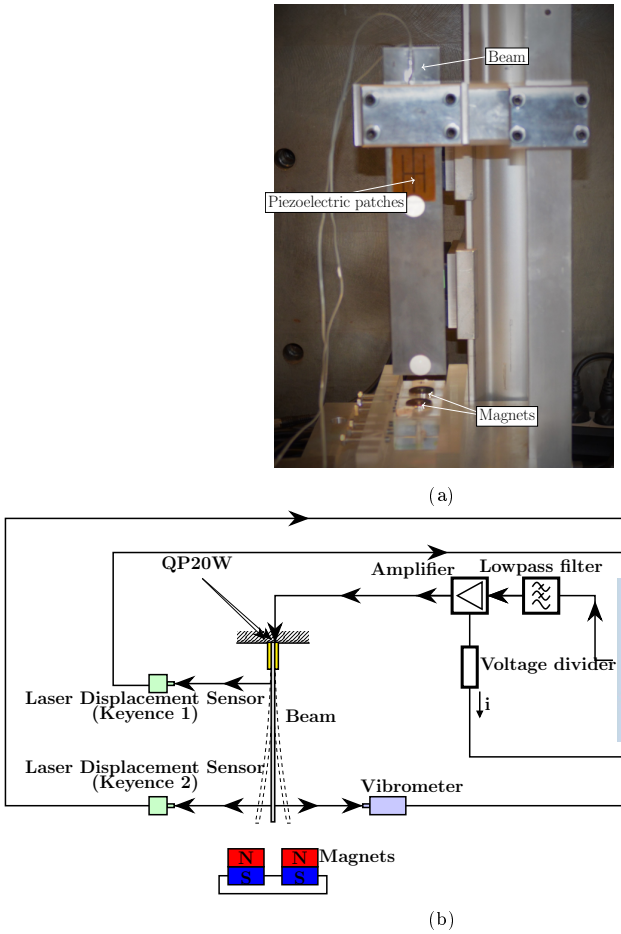

Fig. 4.1: Experimental set-up for the piezomagnetic cantilever beam. (a): Picture of the experiment, showing the piezoelectric patches near the clamped end and the two magnets below the free end. (b): Detailed sketch of the experiment, where RTI stands for real-time interface.

Experimental set-up The set-up is shown in Fig. 4.1. It is a slender steel beam clamped on the upper end to a rigid aluminum frame and free at its lower end. The piezoelectric patches serve as the actuator to excite the beam.

The beam is a stainless steel with dimensions 214 mm × 50 mm × 0.6 mm. Dimensions of the beam were chosen to ensure that the first bending mode is well separated from the torsional and higher bending modes. Hence, it can be assumed that a single nonlinear normal mode will be excited in the vicinity of the fundamental

frequency. A piezoelectric patch *QP20W* is glued on each side near the fixed end of the beam. Two cylindrical neodyne magnets of strength $B = 0.8\,\mathrm{T}$, diameter $d = 25\,\mathrm{mm}$, height $h = 4\,\mathrm{mm}$, equally spaced 17.5 mm from the undeflected beam tip, are positioned 20 mm below the tip of the beam. The poles are aligned as shown in Fig. 4.1 with matching polarity.

Three measurement points were taken: (a) Displacement measurement at 159 mm from the beam tip by a Keyence LK-H152. This serves as the reference measurement. (b) Displacement measurement at 12 mm from the beam tip by a Keyence LK-H152. (c) Velocity measurement at 12 mm by Polytec VibroFlex VFX-F-110 with VibroFlex Neo sensor head. The measurement is on the opposite side of the second Keyence (b).

The PLL and NCPLL models were implemented in Matlab/Simulink and loaded on the real-time controller, dSpace SCALEXIO with sampling rate of 1 kHz. The output is multiplied by a factor of 100 using PI HVPZT Power Amplifier. Due to generated noise in the DAC board of dSpace, a low-pass filter with a cut-off frequency of 200 Hz was placed between the dSpace hardware and the amplifier. The beam is excited via one piezoelectric patch. The NCPLL and PLL algorithm requires as input the actual excitation signal. This is passed from the amplifier to dSpace. A voltage divider (negligible phase error) was used to step down the voltage by a factor of 100, due to the voltage limit of the hardware, 10 V. The assumption of phase-neutral voltage-force transfer in [17] is naturally satisfied with the piezoelectric patches since the force is proportional to the voltage [9]. In the case of electromagnetic exciter, the force is proportional to the current, hence, the assumption will be applicable.

Experimental Procedure and Results An identification of the needed linear characteristics of the system is first performed. Since the nonlinear vibrations of the first bending mode are to be studied, only the eigenfrequency and modal ratio of this fundamental mode are to be identified. Linear vibrations were ensured by using a very small value of excitation amplitude (0.01 V, resulting in 1 V in the piezoelectric patch), leading to a vibration amplitude of the free end tip of about $v(L)/L = 7 \times 10^{-5}$, which in turn gives rise to negligible aerodynamic drag effect. Without the magnets, the first eigenfrequency of the hanging piezoelastic cantilever beam is measured as $\omega_0 = 14.45\,\mathrm{Hz}$, and damping ratio $\xi = 0.6\,\%$. With the two magnets installed, the measurements turns out to $\omega_0 = 14.06\,\mathrm{Hz}$, and the damping ratio is 0.7 %.

From the linear characteristics, the parameters of the NCPLL can be tuned following the method proposed in Section 2.3. The value of the nonlinear controller gain is given from Eq. (1.70) as $K_\mathrm{n} = 3.1895$. However, half of this value, $K_\mathrm{n} = 1.59$, has been used in the experiment which was found to converge faster to the target and within the specified error tolerance. Note that in the present case, since the external excitation is provided by the piezoelectric patches, the beam and the exciter are merged in the same structural elements, and the electrodynamic shaker model used in 1 is not needed, leading to set $\mu_\mathrm{ex} = 0$, and $\delta_\mathrm{p} = \delta_\mathrm{s}$. Table 4.1 summarizes all the values that has been used for the present experimental set-up.

Table 4.1: Parameters for the piezomagnetic beam experiment.

Parameter set	Phase detector	Ω_{ini}	$\omega_\mathrm{c}/\omega_0$	k_p in s $^{-1}$	k_i in s^{-2}	$\bar{\alpha}$	Calculated K_n	Adjusted K_n
NCPLL	$H = 10$	$\omega_0/1.5$	0.5	1 (fixed)	1 (fixed)	5	3.1895	1.59

To draw out some comparisons with a conventional PLL scheme, the gains for the PI-controller has been first set following the method proposed in [17], leading to the values $k_\mathrm{p} = 20.32\ s^{-1}$ and $k_\mathrm{i} = 223.26\ s^{-2}$. This choice however leads to rapid divergence of the controller for the backbone tracking, and manual tuning of the gains through trial and errors has been used. For the experimental continuation of the backbone curve, satisfactory results were obtained by setting $k_\mathrm{p} = 0.5\ s^{-1}$ and $k_\mathrm{i} = 15\ s^{-2}$, leading to stabilization of all periodic orbits along the branch, using step-wise increment of the excitation amplitudes: $\boldsymbol{U} = [0.05 : 0.01 : 3]$ V.

For the frequency response curve, the gains were $k_\mathrm{p} = 0.5\ s^{-1}$ and $k_\mathrm{i} = 5\ s^{-2}$ for phase sweep, $\varphi_\mathrm{ref} \in (0, \pi)$. The calculated gain for the nonlinear controller is sufficient, but to meet the strict error tolerance , $\varepsilon = \pm 0.1°$, it was adjusted for very low amplitudes due to poor signal-to-noise ratio. Amplitude control seems not necessary in this case since the structure is excited via the piezoelectric patches, but there was no need to remove it since it was already implemented in the control loop. The response amplitude is normalized by the length of the beam 214 mm whereas the frequency is normalized by the linear frequency of the piezomagnetoelastic beam, $\omega_0 = 14.06\,\mathrm{Hz}$. Due to experimental conditions, the eigenfrequency can experience slight variations from one experiment to another. Here the curves have been normalized by the eigenfrequency of the current experiment. In general, a good agreement between the two measurements method is found, with a slight discrepancy in the case of the FRC, which might be attributed to the difference in the implemented amplitude control. Interestingly, the conventional PLL has only been able to stabilize the orbits of the FRC starting from $\varphi_{ref} = \pi/12$, leading to a shorter range of available excitation frequency in the resulting solution branch. On the other hand, NCPLL could stabilize orbits from $\varphi_{ref} = \pi$ proving its advantage in situations of poor signal-to-noise ratio.

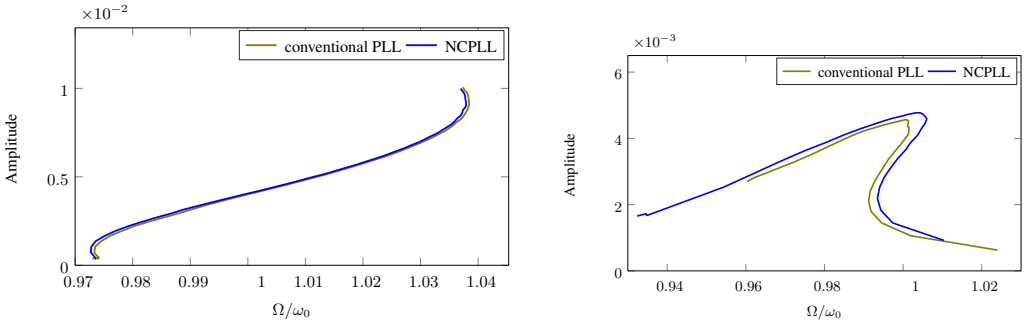

(a) Backbone curve.

(b) Frequency response at 1 V

Fig. 4.2: Comparison of the NCPLL to the conventional PLL. The agreement of the results confirms that the nonlinear controller does not alter the non-invasiveness of the PLL.

Table 4.2 and Table 4.3 summarize the performance of both designs in terms of the settling time and test duration. The time for the trial and error tuning of the conventional PLL is not taken into account. Note that the PLL was started at a higher phase shift in the case of the frequency response curve, yet the NCPLL outperformed it in test duration.

Table 4.2: Backbone curve.

	Start [s]	**Settling [s]**	**Duration [s]**
NCPLL	48.8	7.32	290.91
PLL	64.33	8.30	355.94

Table 4.3: Frequency response curve.

	Start [s]	**Settling [s]**	**Duration [s]**
NCPLL	38.59	9.3	343
PLL	34.39	28.26	479

Another observation is the characteristic softening behaviour at low amplitudes, which was not captured during the linear system identification. This proves again that even at such small amplitudes, some nonlinear phenomena can occur. In this case, it is likely due to the nonlinear property of the piezoelectric patches which was not taken into account and less likely due to micro-slip at the clamped end of the beam. Interestingly, one can note that similar observations at small vibration amplitudes in a PLL experiment have been reported in [12].

The repeatability of the experiment is demonstrated in Fig. 4.3 showing that all points lie within one standard deviation of the mean.

Fig. 4.4 summarizes the obtained results for this case by displaying on the same plot the backbone curve and FRCs for three increasing amplitudes. It can be observed that the backbone curve corresponds well to the peaks of the frequency response curves. By increasing the vibration amplitudes, the overall damping seems also more pronounced, as reported by the shape of the FRCs with a flatter peak. This can be attributed to the increase in aerodynamic drag, see *e.g.* [7] for a more thorough experimental study of the drag-induced damping in large amplitude vibrations of cantilever beams.

4.2 Assembled cantilever beam with bolted joint

Set-up The second experiment involves a cantilever beam with bolted joint providing dry friction contact. Fig. 4.5 shows some pictures of the set-up. The beam parts are held together by two steel bolts, and tightened at torque of 60 Nm. The excitation is targeted at the in-plane mode, imposing shear moments on the bolts. The physical characteristics of the beam are summarized in Table 4.4. The excitation is in this case provided by an electrodynamic shaker. A B&K 4809 shaker has been selected. Following the explanations given in Section 2.4 and Appendix 1, the exciter parameters can be identified and then taken into account to determine the parameters of the control loop.

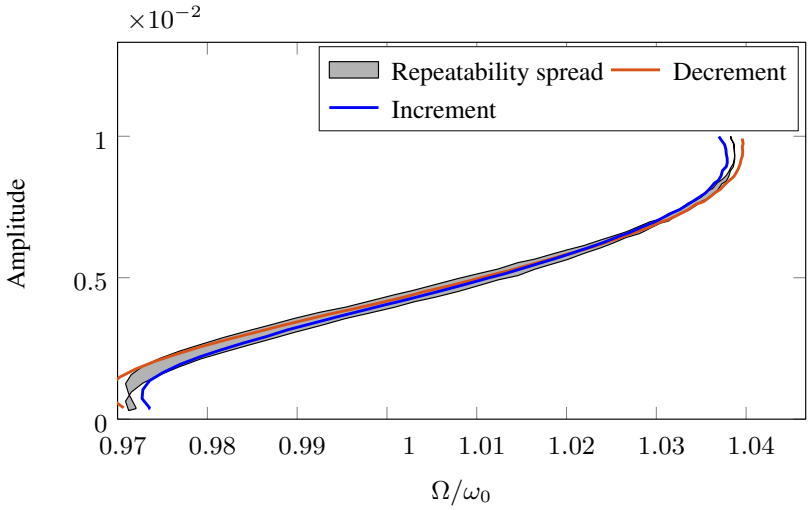

Fig. 4.3: Repeatability of the experiment. Upward and downward excitation sweep results fall within one standard deviation of the mean. Hence, the experiment is independent of the path followed.

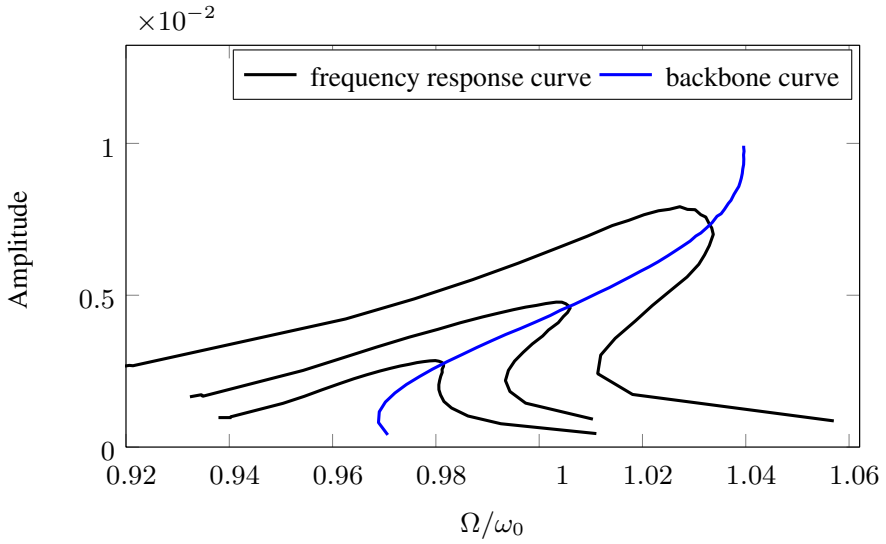

Fig. 4.4: Backbone curve and frequency response. The backbone curve corresponds to the peaks of the frequency response curves with slight deviation at higher amplitudes.

Table 4.4: Physical characteristics of the cantilever beam.

Parameter	Value
Material	Aluminum
Total mass	7.6 kg
Structure	Assembled (bolted)
Thickness	10.34 mm
Width	152 mm
Height	650 mm
Sensor	PCB accelerometers
Number of sensors	6
Tip added mass	2 kg
Shaker	B&K 4809

The calculated value, $K_{\mathrm{n}} = 12.11$ was enough to stabilize the system, but we noticed that at lower excitation amplitudes, there were oscillations about the target which slowed down convergence. Half of this value has been selected for practical reason, in order to improve the convergence speed.

The mode of interest for this particular example is the first in-plane mode. Using low level vibrations and modal identification, the eigenfrequency ω_0 of this mode has been measured such that $\omega_0 = 101.88\,\mathrm{Hz}$. It

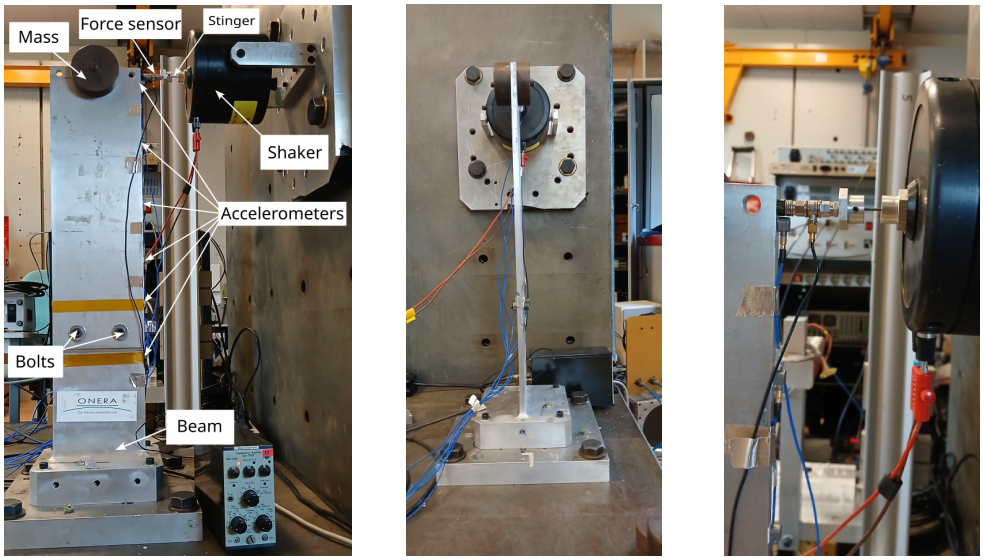

(a) (b) (c)

Fig. 4.5: Experimental set-up of the cantilever beam. (a) Front view. (b) Side view. (c) Close-up view of the upper part showing the excitation.

Table 4.5: Identified linearized plant parameters: Natural frequency = 101.88 Hz

Parameter set	Phase detector	Ω_{ini}	ω_c/ω_0	k_p in s^{-1}	k_i in s^{-2}	$\bar{\alpha}$	Calculated K_n	Adjusted K_n
NCPLL	$H = 10$	$\omega_0/1.5$	0.1	1 (fixed)	1 (fixed)	5	12.11	6.05

corresponds to a much stiffer case as compared to the previous experiment. Parameters for the NCPLL are set according to the linear analysis and the guidelines provided in the previous sections.

Results The results again prove the potential of NCPLL in stabilizing all orbits irrespective of the nonlinearity present. Herein, the NCPLL was able to extract the nonlinear characteristics due to dry friction. A softening characteristics is observed typical of friction damped systems. This confirms the numerical result shown in Section 3.

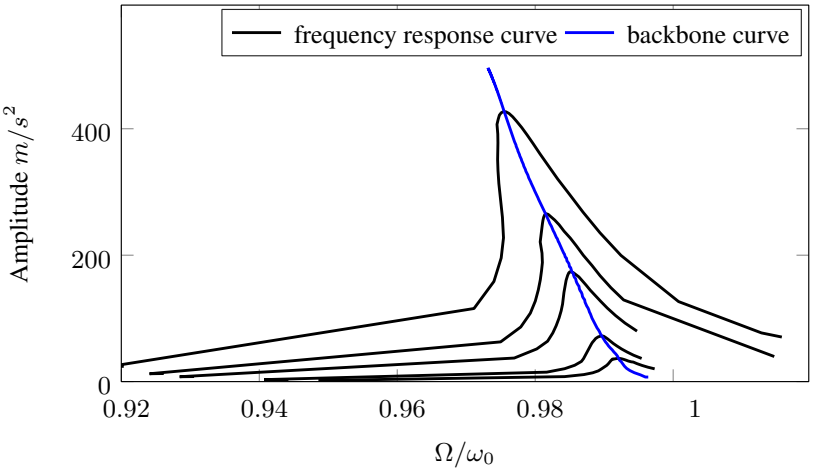

Fig. 4.6: Backbone and frequency response curves of the assembled cantilever beam around its coplanar mode

Backbone and frequency response curves are again extracted for this case. Note that force drop-off in the resonant region is classically observed. To counteract this and to ensure a constant forcing ampitude all along the branches, an additional control loop is inserted in the set-up. Experimental results are reported in Fig. 4.6, showing the excellent ability of the NCPLL in stabilizing all the periodic orbits, irrespective of an a priori

knowledge of the nonlinearity present. In this example, the main nonlinearity is due to the friction occuring the the bolted joint connections, resulting in a clear softening nonlinear characteristics.

The PLL set-up also shows its efficacy in the test duration, since all extracted curves took about 2 minutes of measurements. About 100 points for the backbone curve and 36 points for each of the frequency response curves are measureed along the continuation branch. One of the main advantage of the NCPLL is to demand no further tuning. Once the parameters are set from the linear analysis, then the nonlinear continuation can be done efficiently. From the experimental curves reported in Fig. 4.6, one can observe that, for very small vibration amplitudes, the periodic orbits of the FRCs for phases above 160° has been found unreachable by the present set-up without further change. This failure in the method is here attributed to a poor signal-to-noise ratio at such small vibration levels.

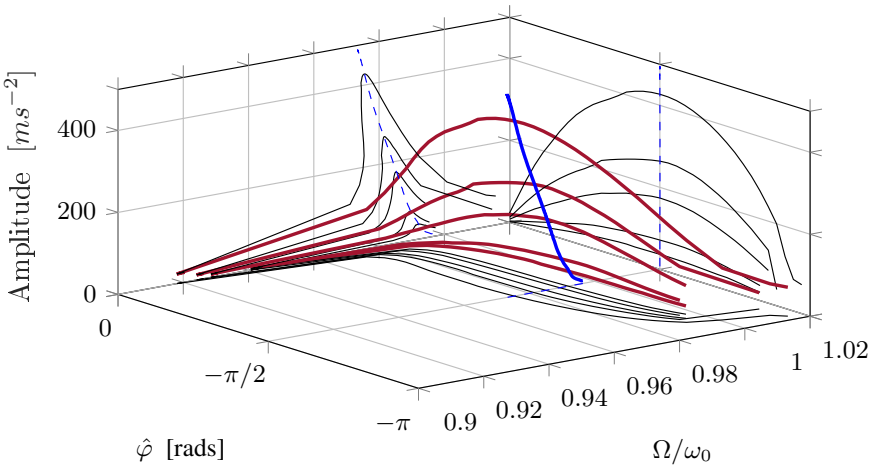

Fig. 4.7: 3D view of the phase-amplitude-frequency relation.

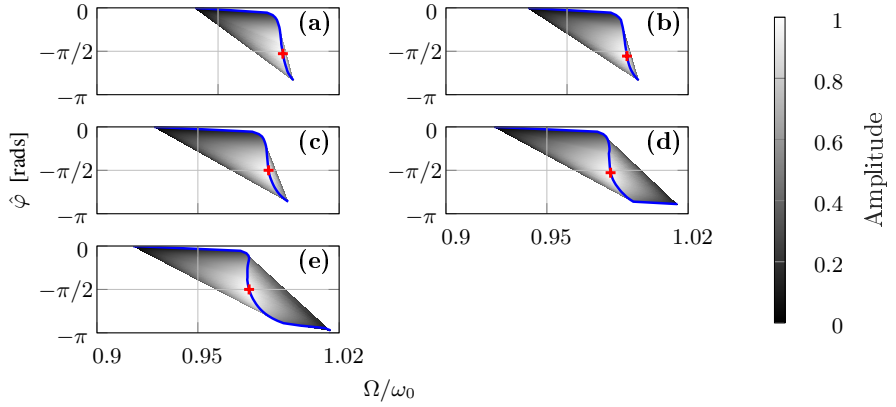

Fig. 4.8: Color map of the phase-amplitude-frequency relation. Red crosses + correspond to the maximum amplitude. Normalized colorbar for the amplitude.

Experimental results are reported in Fig. 4.7 and Fig. 4.8 using a 3-D representation in the space amplitude vs excitation frequency and phase. The backbone curves together with 5 FRCs with increasing amplitudes are reported, and Fig. 4.8 shows the same information in a top view, with gray-shaded area for the amplitudes and the different FRCs in blue. These representations underline how the region with three different solutions is unfolded when using the phase variable, and highlights that the extracted backbone curves exactly corresponds to the prescribed phase lag of $\varphi_{\text{ref}} = \pi/2$.

5 Conclusion

Experimental continuation methods represent a significant advancement and provide access to crucial information about the nonlinear characteristics of systems. They are more and more used in routine experimental

testing and verified as a major tool for having access to the backbone curve and Frequency response functions in structural nonlinear vibrations.

Owing to the tuning effort imposed by control-based methods for the experimental continuation of nonlinear systems, the testing time can be long and the test structure may suffer fatigue due to trial and error. Although successfully applied to simple structures, the tuning effort for Phase-Locked Loop can considerably increase for complex systems. To improve on this, the implementation of a nonlinear controller in the PLL is here proposed. It has been demonstrated numerically and experimentally that NCPLL facilitates the tracking of backbone and frequency response curves, with minimal tuning effort allowing for a fast and robust control. Besides, a systematic approach has been proposed and proven to be useful in diverse situations to give a reliable range for obtaining the optimal gain.

Our design showed notable advantages over the conventional PLL and extends the capability of Phase-Locked Loop testing. On the other hand, Phase-Locked Loop is easier to develop, has been successfully applied to simple structures, but general tuning rules for the involved parameters are lacking and might depend on the type of nonlinearity. Consequently, it is also expected to spend more time in the tuning of the method when handling more complex structures with unknown nonlinearity. The proposed design thus shows notable advantages over the conventional PLL and extends the capability of Phase-Locked Loop testing, improving the duration time and extending the range of available solutions.

We demonstrated the robustness of the NCPLL to noise, and showed that its performance in situations of poor signal-to-noise ratio is remarkable. This capability is very useful in real life applications, as one is not encumbered with the presence of noise. In general, however, it is known that the PLL experiment performs well with quality signal, and the proposed design is not an exception.

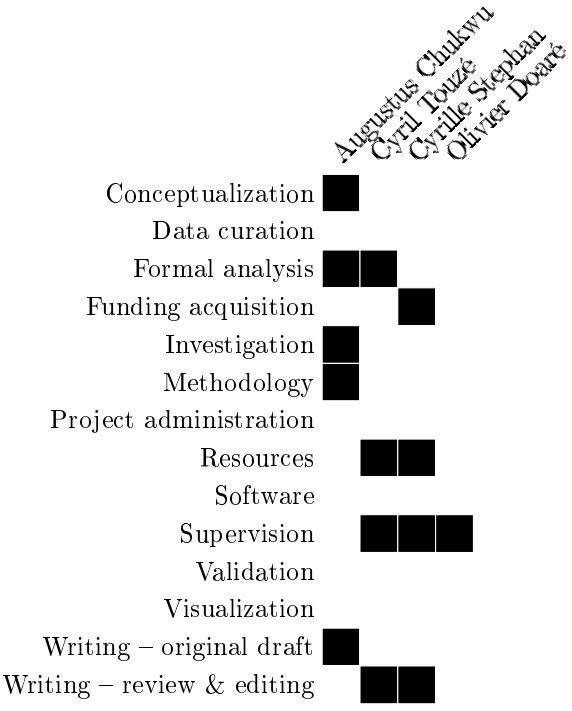

Acknowledgements

This work was supported by the research fund provided by the Direction Générale de l'Aviation Civile (DGAC) of France in the context of the GVT-NEXT project. We thank Prof. Olivier Thomas, Professor of Mechanics and System dynamics, and Head of the research group at LISPEN, Arts et Métiers Institute of Technology, Lille France, for his valuable recommendations toward this work. The authors also thank the reviewers for their valuable comments and suggestions that helped to greatly improve the quality of the manuscript.

References

1. Abeloos, G., Müller, F., Ferhatoglu, E., Scheel, M., Collette, C., Kerschen, G., Brake, M., Tiso, P., Renson, L., Krack, M.: A consistency analysis of phase-locked-loop testing and control-based continuation for a geometrically nonlinear frictional system. Mechanical Systems and Signal Processing **170**, 108820 (2022). https://doi.org/https://doi.org/10.1016/j.ymssp.2022.108820
2. Abeloos, G., Renson, L., Collette, C., Kerschen, G.: Stepped and swept control-based continuation using adaptive filtering. Nonlinear Dynamics **104**(4), 3793–3808 (2021-06-01). https://doi.org/10.1007/s11071-021-06506-z
3. Abramovitch, D.: Phase-locked loops: A control centric tutorial. In: Proceedings of the American Control Conference, May 8–10, 2002 (2020)

4. Atkins, P.A., Wright, J.R., Worden, K.: An Extension Of Force Appropriation To The Identification Of Non-linear Multi-degree Of Freedom Systems. Journal of Sound and Vibration **237**(1), 23–43 (2000-10-12). https://doi.org/10.1006/jsvi.2000.3033
5. Benacchio, S., Malher, A., Boisson, J., Touzé, C.: Design of a magnetic vibration absorber with tunable stiffnesses. Nonlinear Dynamics **85**(2), 893–911 (2016-07-01). https://doi.org/10.1007/s11071-016-2731-3
6. Cochelin, B., Vergez, C.: A high order purely frequency-based harmonic balance formulation for continuation of periodic solutions. Journal of Sound and Vibration **324**(1), 243–262 (2009)
7. Debeurre, M., Benacchio, S., Grolet, A., Grenat, C., Giraud-Audine, C., Thomas, O.: Phase resonance testing of highly flexible structures: Measurement of conservative nonlinear modes and nonlinear damping identification. Mechanical Systems and Signal Processing **215**, 111423 (2024-06-01). https://doi.org/10.1016/j.ymssp.2024.111423
8. Denis, V., Jossic, M., Giraud-Audine, C., Chomette, B., Renault, A., Thomas, O.: Identification of nonlinear modes using phase-locked-loop experimental continuation and normal form. Mechanical Systems and Signal Processing **106**, 430–452 (2018-06-01). https://doi.org/10.1016/j.ymssp.2018.01.014
9. Erturk, A., Inman, D.J.: Introduction to Piezoelectric Energy Harvesting, chap. 1, pp. 1–18. John Wiley & Sons, Ltd (2011). https://doi.org/https://doi.org/10.1002/9781119991151.ch1
10. Ewins, D.J.: Modal testing; theory, practice and application. Research Studies Press, second edition edn. (2000)
11. Fan, M., Clark, M., Feng, Z.C.: Implementation and stability study of phase-locked-loop nonlinear dynamic measurement systems. Communications in Nonlinear Science and Numerical Simulation **12**(7), 1302–1315 (2007-10-01). https://doi.org/10.1016/j.cnsns.2006.01.018
12. Givois, A., Giraud-Audine, C., Deü, J.F., Thomas, O.: Experimental analysis of nonlinear resonances in piezoelectric plates with geometric nonlinearities. Nonlinear Dynamics **102**(3), 1451–1462 (2020). https://doi.org/10.1007/s11071-020-05997-6
13. Givois, A., Tan, J.J., Touzé, C., Thomas, O.: Backbone curves of coupled cubic oscillators in one-to-one internal resonance: Bifurcation scenario, measurements and parameter identification. Meccanica **55**(3), 481–503 (2020-03). https://doi.org/10.1007/s11012-020-01132-2
14. Guckenheimer, J., Holmes, P.: Nonlinear oscillations, dynamical systems and bifurcations of vector fields. Springer-Verlag, New-York (1983)
15. Guillot, L., Cochelin, B., Vergez, C.: A generic and efficient Taylor series-based continuation method using a quadratic recast of smooth nonlinear systems. International Journal for Numerical Methods in Engineering **119**(4), 261–280 (2019)
16. Guillot, L., Lazarus, A., Thomas, O., Vergez, C., Cochelin, B.: A purely frequency based floquet-hill formulation for the efficient stability computation of periodic solutions of ordinary differential systems. Journal of Computational Physics **416**, 109477 (2020). https://doi.org/https://doi.org/10.1016/j.jcp.2020.109477, `https://www.sciencedirect.com/science/article/pii/S0021999120302515`
17. Hippold, P., Scheel, M., Renson, L., Krack, M.: Robust and fast backbone tracking via phase-locked loops. Mechanical Systems and Signal Processing **220**, 111670 (2024-11-01). https://doi.org/10.1016/j.ymssp.2024.111670
18. Hsich, G.C., Hung, J.C.: Phase-locked loop techniques - A survey. IEEE Trnasactions on Industrial Electronics **43**(6), 609–615 (1996)
19. Kamaraj, A.K., Ali, S.F., Arockiarajan, A.: Piezomagnetoelastic broadband energy harvester: Nonlinear modeling and characterization. The European Physical Journal Special Topics **224**, 2803–2822 (2015-11-01). https://doi.org/10.1140/epjst/e2015-02590-8
20. Kerschen, G., Worden, K., Vakakis, A.F., Golinval, J.C.: Past, present and future of nonlinear system identification in structural dynamics. Mechanical System Signal Process **20**(3), 505–592 (2006)
21. Krack, M.: Nonlinear modal analysis of nonconservative systems: Extension of the periodic motion concept. Computers and Structures **154**, 59–71 (2015)
22. Krack, M.: Systems with Contact Nonlinearities. In: Gendelman, O.V., Vakakis, A.F. (eds.) Exploiting the Use of Strong Nonlinearity in Dynamics and Acoustics, pp. 235–272. Springer Nature Switzerland (2024). https://doi.org/$10.1007/978-3-031-56902-9_7$
23. Krack, M., Panning-von Scheidt, L., Wallaschek, J.: On the computation of the slow dynamics of nonlinear modes of mechanical systems. Mechanical Systems and Signal Processing **42**(1–2), 71–87 (2014-01). https://doi.org/10.1016/j.ymssp.2013.08.031
24. Kwarta, M., Allen, M.S.: Nonlinear Normal Mode backbone estimation with near-resonant steady state inputs. Mechanical Systems and Signal Processing **162**, 108046 (2022-01-01). https://doi.org/10.1016/j.ymssp.2021.108046
25. Legrand, M., Pierre, C.: A compact, equality-based weighted residual formulation for periodic solutions of systems undergoing frictional occurrences. Journal of Structural Dynamics pp. 59–71 (2024). https://doi.org/10.25518/2684-6500.190, `https://popups.uliege.be/2684-6500/index.php?id=190`
26. Leine, R., van Campen, D., de Kraker, A., van den Steen, L.: Stick-Slip Vibrations Induced by Alternate Friction Models. Nonlinear Dynamics **16**(1), 41–54 (1998-05-01). https://doi.org/10.1023/a:1008289604683
27. Mojrzisch, S., Twiefel, J.: Phase-controlled frequency response measurement of a piezoelectric ring at high vibration amplitude. Archive of Applied Mechanics **86**(10), 1763–1769 (2016-10-01). https://doi.org/10.1007/s00419-015-1032-5
28. Mojrzisch, S., Wallaschek, J., Bremer, J.: An Experimental Method for the Phase Controlled Frequency Response Measurement of Nonlinear Vibration Systems. Pamm **12**(1), 253–254 (2012). https://doi.org/10.1002/pamm.201210117
29. Moon, F., Holmes, P.: A magnetoelastic strange attractor. Journal of Sound and Vibration **65**(2), 275–296 (1979). https://doi.org/https://doi.org/10.1016/0022-460X(79)90520-0

30. Müller, F., Woiwode, L., Gross, J., Scheel, M., Krack, M.: Nonlinear damping quantification from phase-resonant tests under base excitation. Mechanical Systems and Signal Processing **177**, 109170 (2022-09). https://doi.org/10.1016/j.ymssp.2022.109170
31. Nayfeh, A.H., Mook, D.T.: Nonlinear oscillations. John Wiley & sons, New-York (1979)
32. Nöel, J.P., Kerschen, G.: Nonlinear system identification in structural dynamics: 10 more years of progress. Mechanical Systems and Signal Processing **83**, 2–35 (2017)
33. Peter, S., Leine, R.I.: Excitation power quantities in phase resonance testing of nonlinear systems with phase-locked-loop excitation. Mechanical Systems and Signal Processing **96**, 139–158 (2017)
34. Peter, S., Scheel, M., Krack, M., Leine, R.I.: Synthesis of nonlinear frequency responses with experimentally extracted nonlinear modes. Mechanical Systems and Signal Processing **101**, 498–515 (2018-02-15). https://doi.org/10.1016/j.ymssp.2017.09.014
35. Raze, G., Abeloos, G., Kerschen, G.: Experimental continuation in nonlinear dynamics: recent advances and future challenges. Nonlinear Dynamics **113** (24 March 2025). https://doi.org/10.1007/s11071-024-10543-9
36. Renson, L., Gonzalez-Buelga, A., Barton, D., Neild, S.: Robust identification of backbone curves using control-based continuation. Journal of Sound and Vibration **367**, 145–158 (2016)
37. Renson, L., Shaw, A.D., Barton, D.A.W., Neild, S.A.: Application of control-based continuation to a nonlinear structure with harmonically coupled modes. Mechanical Systems and Signal Processing **120**, 449–464 (2019-04-01). https://doi.org/10.1016/j.ymssp.2018.10.008
38. Scheel, M., Peter, S., Leine, R.I., Krack, M.: A phase resonance approach for modal testing of structures with nonlinear dissipation. Journal of Sound and Vibration **435**, 56–73 (2018)
39. Scheel, M., Weigele, T., Krack, M.: Challenging an experimental nonlinear modal analysis method with a new strongly friction-damped structure. Journal of Sound and Vibration **485**, 115580 (2020-10-27). https://doi.org/10.1016/j.jsv.2020.115580
40. Schwarz, S., Kohlmann, L., Hartung, A., Gross, J., Scheel, M., Krack, M.: Validation of a Turbine Blade Component Test With Frictional Contacts by Phase-Locked-Loop and Force-Controlled Measurements. American Society of Mechanical Engineers Digital Collection (2019-11-05). https://doi.org/10.1115/gt2019-91374
41. Shahruz, S.: Novel phase-locked loops with enhanced locking capabilities. In: Proceedings of the 2002 American Control Conference (IEEE Cat. No.CH37301). vol. 5, pp. 4086–4091 vol.5 (2002-05). https://doi.org/10.1109/acc.2002.1024569
42. Sieber, J., Krauskopf, B.: Control based bifurcation analysis for experiments. Nonlinear Dynamics **51**(3), 365–377 (2008-02-01). https://doi.org/10.1007/s11071-007-9217-2
43. Sieber, J., Krauskopf, B., Wagg, D., Neild, S., Gonzalez-Buelga, A.: Control-based continuation of unstable periodic orbits. Journal of Computational and Nonlinear Dynamics **6**(1), 011005 (09 2010). https://doi.org/10.1115/1.4002101
44. Silva, J.M.M., Maia, N.M.M. (eds.): Modal Analysis and Testing. Springer Netherlands (1999). https://doi.org/10.1007/978-94-011-4503-9
45. Sokolov, I.J., Babitsky, V.I.: Phase Control Of Self-sustained Vibration. Journal of Sound and Vibration **248**(4), 725–744 (2001-12-06). https://doi.org/10.1006/jsvi.2001.3810
46. Sun, X., Horowitz, R., Komvopoulos, K.: Stability and Resolution Analysis of a Phase-Locked Loop Natural Frequency Tracking System for MEMS Fatigue Testing. Journal of Dynamic Systems Measurement and Control-transactions of The Asme - J Dyn Syst Meas Contr **124** (2002-12-01). https://doi.org/10.1115/1.1514658
47. Tam, J.I., Holmes, P.: Revisiting a magneto-elastic strange attractor. Journal of Sound and Vibration **333**(6), 1767–1780 (2014-03-17). https://doi.org/10.1016/j.jsv.2013.11.022
48. Tang, M., Stephan, C., Böswald, M.: Phase resonance method for nonlinear meachanical structures with phase locked loop control. In: Proceedings of ISMA 2020 and USD 2020. pp. 1805–1818 (2020)
49. Tatzko, S., Kleyman, G., Wallaschek, J.: Continuation methods for lab experiments of nonlinear vibrations. GAMM-Mitteilungen **46**(2), e202300009 (2023). https://doi.org/10.1002/gamm.202300009
50. Woiwode, L., Krack, M.: Experimentally uncovering isolas via backbone tracking. Journal of Structural Dynamics (2024)
51. Zhou, T., Kerschen, G.: Identification of secondary resonances of nonlinear systems using phase-locked loop testing. Journal of Sound and Vibration **590**, 118549 (2024). https://doi.org/https://doi.org/10.1016/j.jsv.2024.118549
52. Zhou, T., Raze, G., Kosova, G., Kerschen, G.: Experimental nonlinear modal analysis of an f-16 aircraft using phase-locked loop control. Journal of Aircraft (2025)

Appendices

1 Linear stability analysis of the NCPLL

This appendix is devoted to a linear stability analysis of the Phase-Locked Loop with nonlinear controller. The aim is to derive an analytical expression of the unknown parameter, K_{n} from the linear characteristics of the plant, that is by taking into account the dynamics of the exciter at the attached point. A linear model of an electrodynamic shaker is used. The analysis follows closely with the one reported in [17], which is adapted to insert the nonlinear controller in the loop.

1.1 Exciter-structure modelling

Fig. 1.1 illustrates the exciter-structure coupled dynamics which is expressed in Eq. (1.1) - Eq. (1.6).

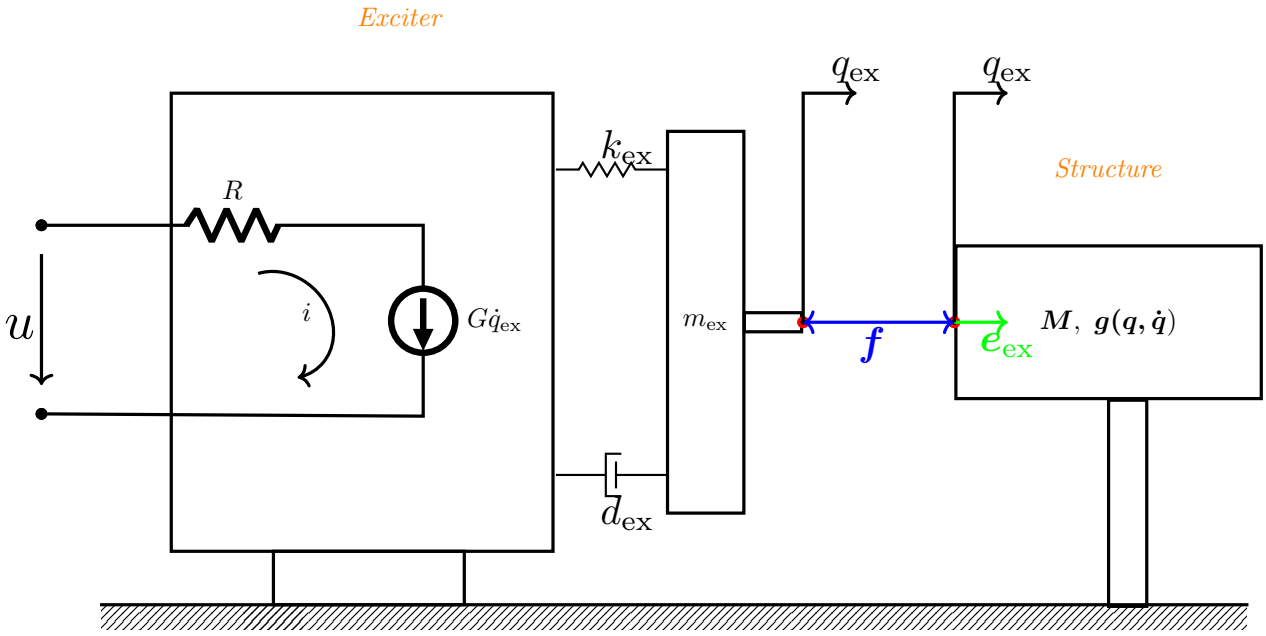

Fig. 1.1: Exciter-structure coupling.

$$m_{\mathrm{ex}}\ddot{q}_{\mathrm{ex}} + d_{\mathrm{ex}}\dot{q}_{\mathrm{ex}} + k_{\mathrm{ex}}q_{\mathrm{ex}} = Gi - f, \tag{1.1}$$

$$Ri + G\dot{q}_{\mathrm{ex}} = u, \tag{1.2}$$

$$q_{\mathrm{ex}} = \boldsymbol{e}_{\mathrm{ex}}^{\top}\boldsymbol{q}. \tag{1.3}$$

where, m_{ex} is the moving mass of the exciter (includes the armature, the coil, sensors and the stinger), k_{ex} is the mechanical stiffness of the exciter, d_{ex} is the damping of the exciter, $G > 0$ is the electromotive force constant, $R > 0$ is the electrical resistance, i is the current and u is the voltage.

The following assumptions underline the exciter-structure coupling dynamics: 1. The exciter structure is assumed rigidly fixed to the ground. 2. Rigid stinger, so that Eq. (1.6) holds. 3. The exciter self-induction is neglected, which physically implies that there is no phase lag between the voltage and the voltage-imposed part of the current [17]. The adaptive filter is governed by Eq. (1.4) - Eq. (1.5),

$$\dot{\hat{F}}^{(h)} = 2\omega_{\mathrm{c}}\mathrm{e}^{-\mathrm{j}h\theta}\left(f - \Re\left\{\sum_{h=0}^{H}\mathrm{e}^{\mathrm{j}h\theta}\hat{F}^{(h)}\right\}\right) \quad h = 0,\ldots,H, \tag{1.4}$$

$$\dot{\hat{Q}}^{(h)} = 2\omega_{\mathrm{c}}\mathrm{e}^{-\mathrm{j}h\theta}\left(q_{\mathrm{ex}} - \Re\left\{\sum_{h=0}^{H}\mathrm{e}^{\mathrm{j}h\theta}\hat{Q}^{(h)}\right\}\right) \quad h = 0,\ldots,H, \tag{1.5}$$

with

$$q_{\mathrm{ex}} = \boldsymbol{e}_{\mathrm{ex}}^{\top}\boldsymbol{q}. \tag{1.6}$$

where $\hat{F}^{(h)}$, and $\hat{Q}^{(h)}$ are the estimates of h-th complex Fourier coefficient of f and q_{ex} respectively, with H the number of harmonics and θ the integral of the the instantaneous frequency Ω as expressed in Eq. (2.5); q_{ex}

is the excitation point, and $\boldsymbol{e}_{\text{ex}}$ is the unit vector in the forcing direction. Integrating both sides of Eq. (1.4) and Eq. (1.5) over one period, Eq. (1.7) and Eq. (1.8) are obtained respectively for $h = 1$. It is then clear that ω_c is the cut-off frequency of the first-order low-pass filters Eq. (1.4) and Eq. (1.5). For what follows, $(\square)_{\text{ex}}$ refer to exciter parameter and $(\hat{\square})$ refer to the estimated quantity. One has:

$$\dot{\hat{F}} = \omega_{\text{c}}(F - \hat{F}), \tag{1.7}$$

$$\dot{\hat{Q}} = \omega_{\text{c}}\left(\psi_{\text{ex}} a \text{e}^{\text{j}\varphi} - \hat{Q}\right), \tag{1.8}$$

where $\psi_{\text{ex}} a$ is the complex Fourier coefficient. In this particular development, it is indeed assumed that the dynamics is contained within a single nonlinear mode; such that it can be parameterized by a single amplitude a and a single phase φ [23].

The dynamics of the structure is described in Eq. (1.9) definition.

$$\boldsymbol{M}\ddot{\boldsymbol{q}} + \boldsymbol{g}(\boldsymbol{q}, \dot{\boldsymbol{q}}) = \boldsymbol{f}(t) \tag{1.9}$$

Following the dynamics of the plant on slow time-scale, the single nonlinear oscillator is approximated by the truncated Fourier-Galerkin projection,

$$\boldsymbol{q} = \Re\left\{\sum_{h=0}^{H} a\boldsymbol{\psi}^{(h)} \text{e}^{\text{j}h(\theta+\varphi)}\right\} \tag{1.10}$$

The modal damping D, the fundamental modal frequency $\omega > 0$, and the Fourier coefficient $\psi^{(h)}$ depend on the modal amplitude a. The mass is normalized, $(\boldsymbol{\psi}^{(1)})^{\mathsf{H}}\boldsymbol{M}\boldsymbol{\psi}^{(1)} = 1$; $\square^{\mathsf{H}}$ is the Hermitian and $\square^{(1)}$ is dropped subsequently for brevity. Inserting Eq. (1.10) into Eq. (1.9) and averaging, gives [17],

$$2\text{j}\Omega(\dot{a} + \text{j}a\dot{\varphi}) + \left(-\Omega^2 + 2D\omega\text{j}\Omega + \omega^2\right) a = \boldsymbol{\psi}^{\mathsf{H}} e_{\text{ex}} F \text{e}^{-\text{j}\varphi}. \tag{1.11}$$

The voltage is given as,

$$u = U\cos(\theta) \tag{1.12}$$

Comparing Eq. (1.1) and Eq. (1.12), the right-hand side of Eq. (1.11) is given by Eq. (1.13)

$$\boldsymbol{\psi}^{\mathsf{H}} e_{\text{ex}} F = \frac{\psi_{\text{ex}} GU}{R} - \left(-\Omega^2 + 2\text{j}\Omega D_{\text{ex}}\omega_{\text{ex}} + \omega_{\text{ex}}^2\right)\mu_{\text{ex}} a \text{e}^{\text{j}\varphi}. \tag{1.13}$$

Here, ω_{ex} and D_{ex} are the exciter natural frequency and the damping ratio of its mechanical part, where $\omega_{\text{ex}} = \sqrt{k_{\text{ex}}/m_{\text{ex}}}$, $2D_{\text{ex}}\omega_{\text{ex}} = (d_{\text{ex}} + G^2/R)/m_{\text{ex}}$, $\mu_{\text{ex}} = \psi_{\text{ex}}^2 m_{\text{ex}}$ which is the modal ratio, and $\psi_{\text{ex}} = \boldsymbol{\psi}^{\mathsf{H}}\boldsymbol{e}_{\text{ex}}$.

1.2 Linearization of the closed loop system

The closed loop system is described by Eq. (2.4) - Eq. (2.12). In the linear case, we can transform the force F and the driving point response Q into the polar form, $F = |F|\text{e}^{\text{j}\varphi_f}$ and $Q = a\psi_{\text{ex}}\text{e}^{\text{j}\varphi}$ and substituting into Eq. (1.4) and Eq. (1.5) respectively, we obtain:

$$\dot{\hat{F}} = \omega_c\left(|F|\text{e}^{\text{j}\varphi_f} - |\hat{F}|\text{e}^{\text{j}\hat{\varphi}_f}\right), \tag{1.14}$$

$$\dot{\hat{Q}} = \omega_c\left(|Q|\text{e}^{\text{j}\varphi} - |\hat{Q}|\text{e}^{\text{j}\hat{\varphi}}\right), \tag{1.15}$$

from which we can deduce the expressions for the phase lags:

$$\dot{\hat{\varphi}}_f = \omega_c\frac{|F|}{|\hat{F}|}\sin\left(\varphi_f - \hat{\varphi}_f\right), \tag{1.16}$$

$$\dot{\hat{\varphi}} = \omega_c\frac{|Q|}{|\hat{Q}|}\sin\left(\varphi - \hat{\varphi}\right). \tag{1.17}$$

Thus, the error variation $\dot{\varepsilon}$ reads

$$\begin{aligned}\dot{\varepsilon} &= -\left(\dot{\hat{\varphi}}_f - \dot{\hat{\varphi}}\right) \\ &= \omega_c\left[\frac{|Q|}{|\hat{Q}|}\sin\left(\varphi - \hat{\varphi}\right) - \frac{|F|}{|\hat{F}|}\sin\left(\varphi_f - \hat{\varphi}_f\right)\right].\end{aligned} \tag{1.18}$$

Linearizing Eq. (1.18) about the fixed point (FP), yields

$$\begin{aligned} \left.\frac{\partial \dot{\varepsilon}}{\partial x}\right|_{\mathrm{FP}} &= \left[\omega_{\mathrm{c}} \frac{\partial}{\partial x}\left(\varphi - \hat{\varphi} - \varphi_f + \hat{\varphi}_f\right)\right]\Big|_{\mathrm{FP}} \\ &= \left[\omega_{\mathrm{c}} \frac{\partial}{\partial x}\left(\varphi - \varphi_f + \varphi_{ref} - \varepsilon\right)\right]\Big|_{\mathrm{FP}}. \end{aligned} \tag{1.19}$$

Finally, the set of ODEs governing the dynamics of the system under the assumption of single nonlinear motion, separative of time scales and linear structure dynamics, write:

$$\dot{a} = -\frac{D\omega + \mu_{\mathrm{ex}} D_{\mathrm{ex}} \omega_{\mathrm{ex}}}{\omega_{\mathrm{c}}} a - \frac{GU\psi_{\mathrm{ex}}}{2\Omega\omega_{\mathrm{c}} R} \sin\varphi, \tag{1.20}$$

$$\dot{\varphi} = \frac{\omega^2 + \mu_{\mathrm{ex}}\omega_{\mathrm{ex}}^2 - \Omega^2(1+\mu_{\mathrm{ex}})}{2\Omega\omega_{\mathrm{c}}} - \frac{GU\psi_{\mathrm{ex}}}{2\Omega\omega_{\mathrm{c}} aR} \cos\varphi, \tag{1.21}$$

$$\dot{\varepsilon} = \varphi - \varphi_f + \frac{\pi}{2} - \varepsilon, \tag{1.22}$$

$$\dot{w} = -\bar{\alpha} w + \bar{\alpha} K_{\mathrm{n}} \tanh\left(\frac{\varepsilon}{\beta}\right), \tag{1.23}$$

$$\dot{I}_w = w. \tag{1.24}$$

Eq. (1.20) and Eq. (1.21) were obtained by substituting Eq. (1.13) into Eq. (1.11) and separating into real and imaginary parts. Importantly, the nonlinear controller is made explicit in Eq. (1.23). Eq. (1.22) involves the phase lag of the excitation with respect to the voltage, φ_f, and thus, must be explicitly expressed in terms of the phase of the response, φ,

$$\varphi_{\mathrm{f}} = \arctan\left(\frac{\Im\{F\}}{\Re\{F\}}\right), \tag{1.25}$$

with,

$$\Re\{F\} = \frac{\psi_{\mathrm{ex}} GU}{R} + \left(\left(\Omega^2 - \omega_{\mathrm{ex}}^2\right)\cos\varphi - 2\Omega D_{\mathrm{ex}}\omega_{\mathrm{ex}}\sin\varphi\right)\mu_{\mathrm{ex}} a \tag{1.26}$$

$$\Im\{F\} = \left(-2\Omega D_{\mathrm{ex}}\omega_{\mathrm{ex}}\cos\varphi + \left(\Omega^2 - \omega_{\mathrm{ex}}^2\right)\sin\varphi\right)\mu_{\mathrm{ex}} a. \tag{1.27}$$

Under the assumption of a phase neutral exciter, that is, $\varphi_{\mathrm{f}} \approx 0$, implies that

$$\mu_{\mathrm{ex}}\left(\omega_{\mathrm{ex}}^2 - \omega^2\right) \approx 0 \tag{1.28}$$

This condition holds if one of the following statements are fulfilled [17]:

- $\mu_{\mathrm{ex}} \approx 0$: the moving mass of the exciter is small and/or the exciter is attached far away from the vibration anti-nodes, and/or
- $\omega_{\mathrm{ex}}^2 \approx \omega^2$: the structure and exciter are frequency matched.

Then, Eq. (1.26) and Eq. (1.27) reduce to Eq. (1.29) and Eq. (1.30) respectively.

$$\Re\{F\} = \frac{\psi_{\mathrm{ex}} GU}{R} \tag{1.29}$$

$$\Im\{F\} = -2\Omega D_{\mathrm{ex}}\omega_{\mathrm{ex}}\mu_{\mathrm{ex}} a\cos\varphi, \tag{1.30}$$

and,

$$\varphi_{\mathrm{f}} = \left(\frac{-2\Omega D_{\mathrm{ex}}\omega_{\mathrm{ex}}\mu_{\mathrm{ex}} a\cos\varphi}{\frac{\psi_{\mathrm{ex}} GU}{R}}\right) \tag{1.31}$$

We can now insert Eq. (1.31) into Eq. (1.22) to obtain the new set of ODEs Eq. (1.43) - Eq. (1.47).

1.3 Asymptotic behaviour around the locked state:

The locked state corresponds to a fixed point where by definition the time derivatives vanish, yeilding the following set of equations:

$$
\begin{aligned}
0 &= \varepsilon, && (1.32)\\
0 &= y, && (1.33)\\
0 &= w, && (1.34)\\
I_w &= \Omega - \Omega_{\mathrm{ini}}, && (1.35)\\
0 &= \frac{\pi}{2} - (\hat{\varphi}_f - \hat{\varphi}), && (1.36)\\
\hat{F} &= F = |F|\mathrm{e}^{\mathrm{j}\varphi_f}, && (1.37)\\
\hat{Q} &= \psi_{\mathrm{ex}} a \mathrm{e}^{\mathrm{j}\varphi}, && (1.38)\\
\hat{\varphi} &= \varphi, && (1.39)\\
\hat{\varphi}_f &= \varphi_f, && (1.40)\\
\Omega &= \omega && (1.41)\\
2D\omega^2 a &= \psi_{\mathrm{ex}}|F|. && (1.42)
\end{aligned}
$$

Again, the assumption of the single nonlinear mode vibration allows expressing the dynamics of the structure with (a, φ). At low excitation regime, one can reduce the system state-space such that complex state variables $\hat{F}$ and $\hat{Q}$ are replaced by the control error, ε. This gives the following system of linear autonomous ordinary equations:

$$
\begin{aligned}
\dot{a} &= -\frac{D\omega + \mu_{\mathrm{ex}} D_{\mathrm{ex}} \omega_{\mathrm{ex}}}{\omega_{\mathrm{c}}} a - \frac{GU\psi_{\mathrm{ex}}}{2\Omega\omega_{\mathrm{c}} R} \sin\varphi, && (1.43)\\
\dot{\varphi} &= \frac{\omega^2 + \mu_{\mathrm{ex}}\omega_{\mathrm{ex}}^2 - \Omega^2(1+\mu_{\mathrm{ex}})}{2\Omega\omega_{\mathrm{c}}} - \frac{GU\psi_{\mathrm{ex}}}{2\Omega\omega_{\mathrm{c}} a R} \cos\varphi, && (1.44)\\
\dot{\varepsilon} &= \varphi + \frac{2R\Omega D_{\mathrm{ex}}\omega_{\mathrm{ex}}\mu_{\mathrm{ex}} a}{\psi_{\mathrm{ex}} GU} \cos\varphi + \frac{\pi}{2} - \varepsilon, && (1.45)\\
\dot{w} &= -\bar{\alpha} w + \bar{\alpha} K_{\mathrm{n}} \varepsilon, && (1.46)\\
\dot{\bar{I}}_w &= w. && (1.47)
\end{aligned}
$$

Noting that $\varepsilon << \beta$. The linearized ODEs around the locked state is the deviation $\Delta\boldsymbol{z}$ from the fixed point of the state $\boldsymbol{z} = [a; \varphi; \varepsilon; w; \bar{I}_w]$, thus,

$$
\begin{aligned}
\Delta\boldsymbol{z}' &= \left.\frac{\partial f}{\partial \boldsymbol{z}}\right|_{FP} \Delta\boldsymbol{z}, && (1.48)\\
\Delta\boldsymbol{z}' &= \boldsymbol{A_0}\Delta\boldsymbol{z}, && (1.49)\\
f &= \begin{bmatrix} \dot{a} \\ \dot{\varphi} \\ \dot{\varepsilon} \\ \dot{w} \\ \dot{\bar{I}}_w \end{bmatrix}, && (1.50)
\end{aligned}
$$

$$
\boldsymbol{A_0} = \begin{bmatrix}
-\bar{\delta}_{\mathrm{p}} & 0 & 0 & -\bar{\Upsilon} & -\bar{\Upsilon} \\
0 & -\bar{\delta}_{\mathrm{p}} & 0 & -\bar{\mu} & -\bar{\mu} \\
0 & \dfrac{\delta_{\mathrm{p}}}{\delta_{\mathrm{s}}} & -1 & 0 & 0 \\
0 & 0 & \bar{\alpha} K_{\mathrm{n}} & -\bar{\alpha} & 0 \\
0 & 0 & 0 & 1 & 0
\end{bmatrix} \qquad (1.51)
$$

with

$$\delta_{\mathrm{s}} = (D\omega)_{\mathrm{lin}}\,, \tag{1.52}$$
$$\delta_{\mathrm{p}} = \delta_{\mathrm{s}} + (\mu_{\mathrm{ex}} D_{\mathrm{ex}} \omega_{\mathrm{ex}})_{\mathrm{lin}}\,, \tag{1.53}$$
$$\bar{\delta}_{\mathrm{p}} = \frac{\delta_{\mathrm{p}}}{\omega_{\mathrm{c}}}, \tag{1.54}$$
$$\bar{\alpha} = \frac{\alpha}{\omega_{\mathrm{c}}}, \tag{1.55}$$
$$\bar{\mu} = \frac{(1+\mu_{\mathrm{ex}})_{\mathrm{lin}}}{\omega_{\mathrm{c}}}, \tag{1.56}$$
$$\bar{\Upsilon} = \frac{GU}{2R\omega_{\mathrm{c}}} \left(\frac{\psi_{\mathrm{ex}}}{\omega^2}\right)_{\mathrm{lin}}. \tag{1.57}$$

Obviously, the phase does not depend on the amplitude, so the matrix $\boldsymbol{A}_0$ is reduced to

$$\boldsymbol{B_0} = \begin{bmatrix} -\bar{\delta}_{\mathrm{p}} & 0 & -\bar{\mu} & -\bar{\mu} \\ \dfrac{\delta_{\mathrm{p}}}{\delta_{\mathrm{s}}} & -1 & 0 & 0 \\ 0 & \bar{\alpha} K_{\mathrm{n}} & -\bar{\alpha} & 0 \\ 0 & 0 & 1 & 0 \end{bmatrix} \tag{1.58}$$

and Eq. (1.49) is reduced to Eq. (1.59)

$$\Delta \boldsymbol{y}' = \boldsymbol{B_0} \Delta \boldsymbol{y} \tag{1.59}$$

with $y = y(\varphi; \varepsilon; w; \bar{I}_{\mathrm{w}})$. The determinant of $(\boldsymbol{B_0} - \lambda I) = 0$, then,

$$a_0\lambda^4 + a_1\lambda^3 + a_2\lambda^2 + a_3\lambda + a_4 = 0 \tag{1.60}$$

$$a_0 = 1 \tag{1.61}$$
$$a_1 = 1 + \bar{\alpha} + \bar{\delta}_{\mathrm{p}} \tag{1.62}$$
$$a_2 = \bar{\alpha}\bar{\delta}_{\mathrm{p}} + \bar{\alpha} + \bar{\delta}_{\mathrm{p}} \tag{1.63}$$
$$a_3 = \bar{\alpha}\bar{\delta}_{\mathrm{p}} + \bar{\mu}\bar{\alpha} K_{\mathrm{n}} \frac{\delta_{\mathrm{p}}}{\delta_{\mathrm{s}}} \tag{1.64}$$
$$a_4 = \bar{\mu}\bar{\alpha} K_{\mathrm{n}} \frac{\delta_{\mathrm{p}}}{\delta_{\mathrm{s}}} \tag{1.65}$$

which gives four eigenvalues whose real parts must be negative to have asymptotic stability. The phase transient will quickly decay when the maximum real part among the eigensolutions is minimized [17].

The Routh-Hurwitz stability criterion states that for the system to be stable and since $a_0 > 0$, the Eq. (1.66) - Eq. (1.69) must hold.

$$a_1 > 0 \tag{1.66}$$
$$a_1 a_2 - a_0 a_3 > 0 \tag{1.67}$$
$$(a_1 a_2 - a_0 a_3)\, a_3 - a_1^2 a_4 > 0 \tag{1.68}$$
$$a_4 > 0 \tag{1.69}$$

Eq. (1.66) and Eq. (1.69) are naturally satisfied by construction. If Eq. (1.68) holds, Eq. (1.67) is automatically satisfied. From the solution to Eq. (1.68), we establish the relation:

$$K_{\mathrm{n}} < \frac{\Lambda + \sqrt{\Lambda^2 + 4\left(\bar{\mu}\bar{\alpha}\dfrac{\delta_{\mathrm{p}}}{\delta_{\mathrm{s}}}\right)^2 \Theta}}{2\left(\bar{\mu}\bar{\alpha}\dfrac{\delta_{\mathrm{p}}}{\delta_{\mathrm{s}}}\right)^2}, \tag{1.70}$$

where the following parameters have been defined as:

$$\Lambda = \bar{\mu}\bar{\alpha}\frac{\delta_\mathrm{p}}{\delta_\mathrm{s}}\left(\Pi - a_1^2 - 2\bar{\alpha}\bar{\delta}_\mathrm{p}\right), \tag{1.71a}$$

$$\Theta = \bar{\alpha}\bar{\delta}_\mathrm{p}\left(\Pi - \bar{\alpha}^2\bar{\delta}_\mathrm{p}\right), \tag{1.71b}$$

$$\Pi = a_1 a_2. \tag{1.71c}$$

The term $\frac{\delta_\mathrm{p}}{\delta_\mathrm{s}}$ is the ratio of the coupled exciter and shaker linear damping coefficient to the linear damping coefficient of the structure only, at the excitation point. $\left(\bar{\square}\right)$ indicates quantities that have been normalized by the adaptive filter cut-off frequency ω_c, and $\bar{\mu}$ is the normalized mass ratio at the excitation point. A plot of K_n with respect to $\bar{\alpha}$ is given in Fig. 1.2 which shows a linear relationship. The other parameters have been set as those reported in Section 3.1..

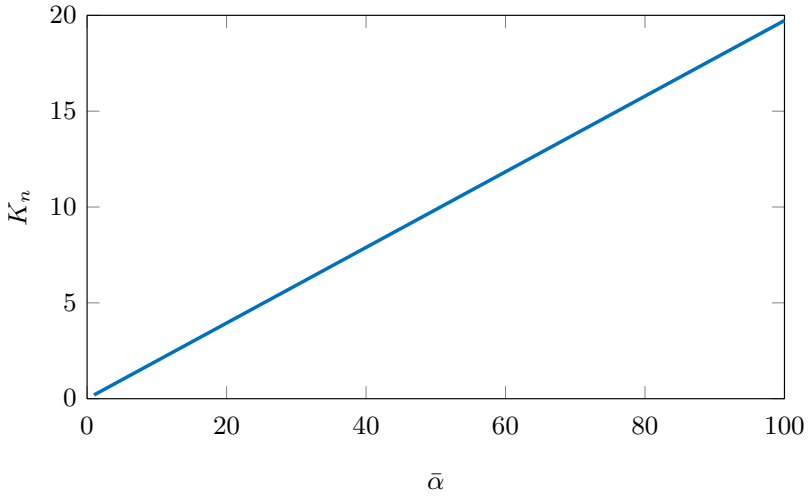

Fig. 1.2: Variation of K_n with respect to $\bar{\alpha}$.

What is observed is a linear relationship, indicating that K_n tends to infinity in the limit of large $\bar{\alpha}$ suggesting that the upper bound can be shifted to arbitrary large values by increasing $\bar{\alpha}$. Practically, this cannot be the case because K_n serves, as shown in Eq. (1.46), as a proportional gain, such that selecting too large a value will destabilize the system due to large perturbation from the stationary point. To further investigate this problem, we removed the low-pass filter and conducted again the stability analysis of this new configuration which shows that as long as $K_\mathrm{n} > 0$, the system is stable. For, this reason, it appears analytically (and numerically consistent), that setting $K_\mathrm{n} = 1$, is sufficient for stability. We recommend to avoid too large values of K_n to prevent large perturbations of the system dynamics, especially during the transients. By using Eq. (1.70), an initial value can be obtained which can be reduced if the error is large.

Finally, it should be mentioned that the low-pass filter is generally used as a security in the NCPLL scheme. For low frequencies, there might be no obvious advantages brought about by the low-pass filter. On the other hand, its effect shall be more important for high frequencies, as also indicated in [41].

2 Further comparisons of NCPLL with PLL on the Duffing oscillator

The comparisons between the results that can be obtained with either the NCPLL or a standard PLL procedure are here further commented on for the Duffing oscillator, following the results shown in Section 3.1. The parameters of the Duffing equation have been left unchanged as compared to Section 3.1.

Fig. 2.1 first shows how a conventional PLL with linear PI controller compares to the NCPLL algorithm. The forcing amplitue has now been set to $F = 100$ N (the maximum value used in the main text was 10 N). The PI gains of the standard PLL are those provided in [8]. Results shown in Fig. 3.4 already highlighted that without further tuning, the PLL encountered extreme difficulties in stabilizing the periodic orbits for $F = 10$ N. In [8], fully stabilized result are proposed because continuous sweeps of the force and the phase are used, in contrary to the step-wise changes adopted in the present study. Increasing the forcing to 100 N makes the convergence even more difficult and the PLL is found to be unable to recover the FRC without further tuning, highlighting that the settings needed for the PLL algorithm needs to be constantly adjusted in order to face the varying nonlinear characteristics. On the other hand, and without any further tuning, the NCPLL continues

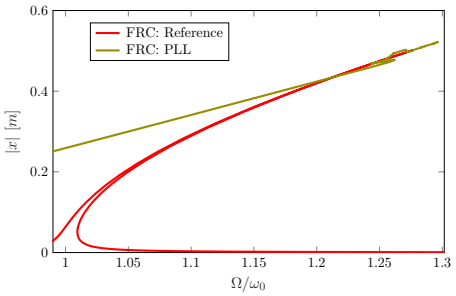

(a) Conventional PLL.

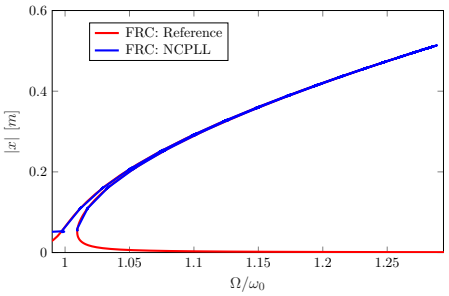

(b) NCPLL

Fig. 2.1: Frequency response curve for the Duffing oscillator with a forcing amplitude of $F = 100$ N. (a) a conventional PLL architecture with gains set as $k_\mathrm{p} = 0.5\ \mathrm{s}^{-1}$, and $k_\mathrm{i} = 10$ s. (b) NCPLL. A reference solution obtained by numerical continuation as implemented in the software MANLAB is also shown in red.

to provide an accurate result and is able to recover the FRC with such large amplitude, with a frequency shift of the nonlinear frequency which is about 28% in this specific case. Of course the PLL is in principle able to recover such responses, but this case study underlines that a proper tuning of the gains is needed which might importantly vary depending on the experimental conditions.

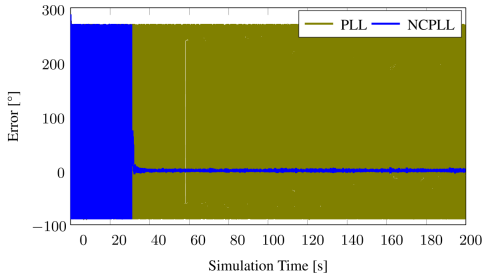

(a) Error signal for $SNR = 5$.

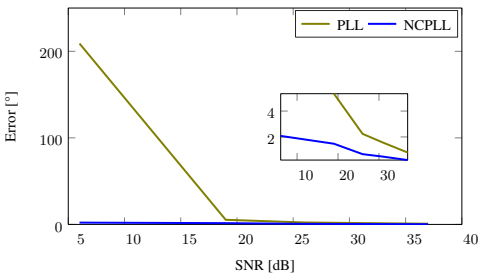

(b) Effect of noise on both designs.

Fig. 2.2: Robustness to noise. NCPLL shows better handling of noise.

The comparison of the two designs is now discussed by comparing the effect of noise. Fig. 2.2 highlights that the NCPLL is much more robust to adding noise to the signal to continue the solution branches. Even in such adverse condition where the signal-to-noise ratio (SNR) is about 5dB, the NCPLL shows ability to stabilize the orbits and meet the tolerance criterion. On the other hand, for such level of noise, the PLL without further tuning has been shown unable to recover solutions, and the SNR needs to fall down to 20dB for the PLL to meet the error tolerance.

Further analysis of both designs prove that the NCPLL locks faster to the target, hence facilitating testing time, which is illustrated in Fig. 2.3. The NCPLL tracked the backbone curve under 800 s (simulation time), and kept the error below the specified tolerance throughout the simulation. On the other hand, the PLL without further tuning needs a much larger operating time, demanding for more than 3400 s to follow the backbone curve, while continuously showing large oscillations about the target. This highlights that further tuning is definitely needed for the PLL to work out efficiently, asking for more dedicated operating instructions for the users to be able to tune the PI gains depending on available characteristics of the experiments.

One notable advantage of the NCPLL is that the same obtained gains for the tracking of the backbone curve can be used to track the complete orbits of the frequency response curve as shown in the above examples. This is remarkable as there will be no need to select different gains for different phase targets, especially for unstable orbits. The error is kept minimal for each forcing level as shown in Fig. 2.3 which improves the speed of the algorithm. The first 20 s indicates time taken to converge to the target. As amplitude increases, the signal quality improves and large error variations cancel out. In general, convergence is fast, and the NCPLL maintains smooth continuation along the curve.

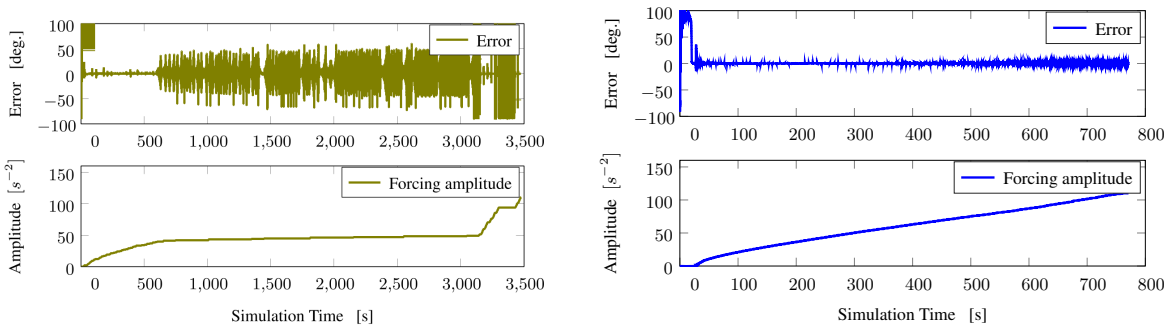

(a) Error signal with PLL.

(b) Error signal with NCPLL.

Fig. 2.3: Comparison of error signals over the simulation duration.